Molecular dynamics simulation of the fragile glass-former orthoterphenyl: A flexible molecule model

S. Mossa,[1] R. Di Leonardo,[1] G. Ruocco,[1] and M. Sampoli[2]
[1]*Dipartimento di Fisica and INFM, Università di L'Aquila, Via Vetoio, Coppito, L'Aquila, I-67100, Italy*
[2]*Dipartimento di Energetica and INFM, Università di Firenze, Via Santa Marta 3, Firenze, I-50139, Italy*
(Received 16 December 1999)

We present a realistic model of the fragile glass-former orthoterphenyl and the results of extensive molecular dynamics simulations in which we investigated its basic static and dynamic properties. In this model the internal molecular interactions between the three rigid phenyl rings are described by a set of force constants, including harmonic and anharmonic terms; the interactions among different molecules are described by Lennard-Jones site-site potentials. Self-diffusion properties are discussed in detail together with the temperature and momentum dependencies of the self-intermediate scattering function. The simulation data are compared with existing experimental results and with the main predictions of the mode-coupling theory.

PACS number(s): 64.70.Pf, 71.15.Pd, 61.25.Em, 61.20.−p

I. INTRODUCTION

In recent years a renewed interest on the glass transition phenomenon has motivated extensive experimental and theoretical works (see [1] and reference therein). On the theoretical side, new descriptions of the glass transition have been developed: they emphasized either the dynamic [as the mode-coupling theory (MCT) of Götze [2] (the reader may also consult Ref. [3]) and Schilling and Kob [3] or the coupled oscillators model of Ngai and Tsang [4]] or the thermodynamic (as the first principle computation based on a replica formulation of [5] or the inherent structure formalism computation of [6]) aspects of the transition itself.

A common feature of all these theories is they have been developed for ''model systems,'' often monoatomic models. The comparison of the theoretical results with the real experiment are, therefore, complicated by the trivial observation that in the real world the glass-forming systems are made out of ''molecular systems.'' As a consequence in the current literature there is a large debate on the applicability of the theoretical predictions to the experimental outcome and the more stringent tests of the theories come from molecular dynamics (MD) works.

As an example, it is highly debated in literature the origin, in a molecular glass former, of *secondary* relaxations that can be observed by several experimental techniques beside the well-known microscopic and structural dynamics (see, among others, Ref. [7] and references therein). For instance, *fast* relaxations (i.e., in the 10^{-12} s range) have been observed in several glasses and it is not yet clear if their origin is related to the molecular center of mass motion, as MCT would explain in terms of the β process, or rather to rotational or intramolecular dynamics. It is clear the crucial role that MD simulations can play to solve this specific problem. If it is possible to build a *realistic* model able to take into account the internal degrees of freedom, as well as the translational dynamics, computer simulations allow one to access any observable quantity of the system, and also those not directly measurable by present experimental techniques. Such possibility, together with the physical intuition, could allow the identification of the microscopic mechanisms underlying the different observed relaxation processes.

In this paper we want to address the problem to set up a ''realistic'' potential for a glass model system capable of accounting for the internal molecular degrees of freedom. Among the glass-forming molecular liquids characterized by an extremely rich dynamical behavior, the organic *fragile* [1] glass former *orthoterphenyl* (OTP) ($T_m = 329$ K, $T_c \simeq 290$ K, $T_G = 243$ K) has received much attention from both experimental and numerical simulation points of view. The structure of the OTP molecule, shown in Fig. 1, is known from neutron [8] and x-ray [9] diffraction studies; in condensed state the OTP molecules are bound together only by van der Waals forces, which resemble the Lennard-Jones ones often used by most theories and computer simulations aiming to study the glass transition problem.

Due to its structural complexity, if we would like to obtain reliable results to be compared with experimental data we need to take into account not only the translations of the molecular center of masses and the rotations of the molecules as a whole, but also intramolecular motions like stretching along the molecular bonds, tilt of the bonds, rotation of the side rings with respect to the central one, and so on. In other words, we need to describe the dynamics of the liquid at the *atomic* level. On the contrary, in order to set up

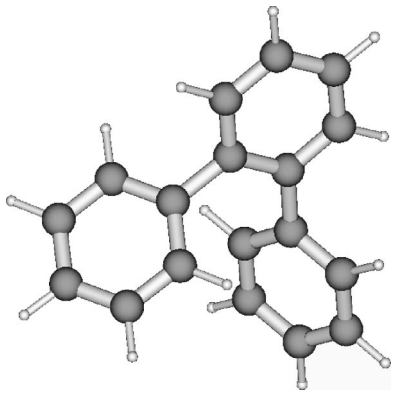

FIG. 1. Molecular structure of OTP ($C_{18}H_{14}$); it is constituted by three phenyl rings, the two side rings being attached to the parent (i.e., central) ring by covalent bonds.

a computational scheme which is affordable in not-too-long time with the nowadays computer capability, we need the *simplest* model potential able to capture the relevant features of the dynamical behavior of the real system.

In the literature numerical studies of OTP have been proposed making use of different techniques ranging from *harmonic lattice dynamics* [10] to molecular dynamics simulations on the atomic level based on a general force field provided by the standard program Alchemy III [11]. Nevertheless, to our knowledge, only two studies based on molecular dynamics simulations of *molecular models* of OTP have been proposed so far. They are as follows.

(i) Lewis and co-workers [12,13] represent the molecule like a three-sites complex, each site playing the role of a whole phenyl ring, without internal dynamics and an intermolecular interaction of the Lennard-Jones (LJ) type. This model takes into account only the dynamical behavior associated with the translations of the molecular center of masses and with the rotations of the molecules as a whole.

(ii) Kudchadkar and Wiest [14] propose a more realistic model with the ''true'' structure of the molecule. The intermolecular interaction is of LJ type and, as internal degrees of freedom, only the rotational dynamics of the side rings with respect to the central one is taken into account. These internal degrees of freedom are effectively the most relevant; nevertheless, the authors parametrize the potential in such a way that the side rings are, at equilibrium, in a configuration that corresponds to a saddle point in the molecular energy surface.

The model potential we are going to introduce is much more efficient in mimicking the complexity of the dynamical behavior of the real system. The paper is organized as follows: in Sec. II we introduce the intramolecular model potential; in Sec. III we explain how we calculated the force constants in order to reproduce a realistic isolated molecule vibrational spectrum. In Sec. IV we present some computational details and in Sec. V we note some of the main well-established predictions of the ideal mode-coupling theory used in Sec. VI to test the center of mass dynamical behavior. In Sec. VI we discuss our MD simulation results mainly with regard to the study of the diffusion and self-dynamic properties. Section VII contains an overall discussion and the conclusions.

II. THE MOLECULAR MODEL

In our model the OTP molecule is constituted by three *rigid* hexagons (phenyl rings) of side $L_a=0.139$ nm connected as shown in Fig. 1, i.e., two adjacent vertices of the *parent* (central) ring are bonded to one vertex of the two *side* rings by bonds whose length, at equilibrium, is $L_b=0.15$ nm. In our scheme, each vertex of the hexagons is thought to be occupied by a fictious atom of mass $M_{\mathrm{CH}}=13$ amu representing a carbon-hydrogen pair (C-H). The choice of such a fictious atom, with its renormalized mass, greatly simplifies the computer simulation but presents some drawbacks: (i) in the real molecule the two couples of carbon atoms connecting the rings are not bonded to hydrogen atoms, while in our model we consider all the 18 vertices having the same mass M_{CH} so that the total molecular mass is overestimated (234 rather than 230 amu) and (ii) the moments of inertia of the model rings are smaller than the real ones the hydrogen atoms being too close to the ring center. Nevertheless, we expect only minor effects on the overall dynamics from the previous simplification.

The three rings of a given molecule interact among themselves by an *intramolecular* potential, such potential being chosen (i) to preserve the molecule from ''dissociation;'' (ii) to give the correct relative equilibrium positions for the three rings; and (iii) to represent the real intramolecular vibrational spectrum as close as possible. The interaction among different molecules, actually among the rings pertaining to different molecules, is accounted for by a site-site pairwise additive potential energy of the (6-12) Lennard-Jones type, each site being one of the hexagons vertices.

To sum up, the total interaction potential energy is written as the sum of an *intermolecular* and an *intramolecular* term,

$$V_{tot}=V_{inter}+V_{intra}. \tag{1}$$

The first term can be written explicitly as

$$V_{inter}=\frac{1}{2}\sum_{i\neq j}\sum_{\xi\xi'}\sum_{\ell\ell'}V_{LJ}(|\overline{r}_{i\xi\ell}-\overline{r}_{j\xi'\ell'}|), \tag{2}$$

where $\overline{r}_{i\xi\ell}$ is the position of the ℓth atom ($\ell=1,\ldots,6$) in the ξth ring ($\xi=1,\ldots,3$, hereafter $\xi=1$ indicates the parent ring) belonging to the ith molecule ($i=1,\ldots,N$), and

$$V_{LJ}(R)=4\epsilon\left[\left(\frac{\sigma}{R}\right)^{12}-\left(\frac{\sigma}{R}\right)^{6}\right]. \tag{3}$$

The optimal choice of the two intermolecular force parameters, ϵ and σ, will be discussed later.

In principle, the *intramolecular* interaction potential can be expressed in terms of the degrees of freedom describing the center of mass positions ($\overline{R}_\xi$, $\xi=2,3$) and orientations (e.g., the set of Eulerian angles) of the side rings with respect to the parent ring. However, for computational purposes, it is simpler to express the intramolecular potential in terms of orthonormal unit vectors attached to each ring or better in terms of quantities built from these vectors. With reference to Fig. 2 the sets of unit vectors for each ring $\{\hat{l}_\xi,\hat{m}_\xi,\hat{n}_\xi\}$ are defined as

$$\hat{l}_\xi=(1,0,0),$$

$$\hat{m}_\xi=(0,1,0),$$

$$\hat{n}_\xi=(0,0,1),$$

i.e., $\hat{l}_\xi$ and $\hat{m}_\xi$ are orthogonal unit vectors in the ring plane, while $\hat{n}_\xi$ is the normal to that plane.

The unit vectors that are parallel to the ring-ring bonds at equilibrium are given by

$$\overline{u}_2=\tfrac{1}{2}(\hat{l}_2+\sqrt{3}\hat{m}_2),$$

$$\overline{u}_3=\tfrac{1}{2}(-\hat{l}_3+\sqrt{3}\hat{m}_3),$$

$$\overline{u}_{1(2)}=\tfrac{1}{2}(\hat{l}_1+\sqrt{3}\hat{m}_1),$$

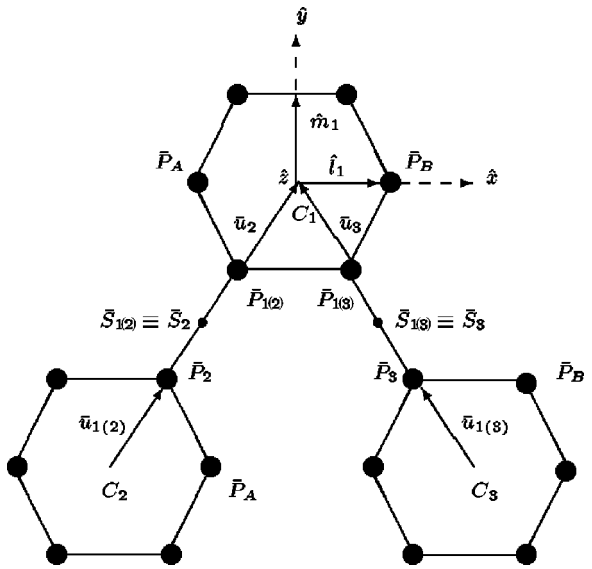

FIG. 2. Model geometry: each phenyl ring is represented by a rigid hexagon of side $L_a = 0.139$ nm and the equilibrium bond length is $L_b = 0.150$ nm. C_1, C_2, C_3 represent the origins of the reference frames fixed with the rings; $\bar{u}_2, \bar{u}_3, \bar{u}_{1(2)}, \bar{u}_{1(3)}$ are the vectors parallel to the ring bonds; $\hat{l}_1$ and $\hat{m}_1$ are two versors identifying the parent ring plane; $\bar{P}_2, \bar{P}_3, \bar{P}_{1(2)}, \bar{P}_{1(3)}$ are the positions of the carbon atoms bonding together the rings; $\bar{S}_2, \bar{S}_3, \bar{S}_{1(2)}, \bar{S}_{1(3)}$ are four interaction sites introduced to force the rings towards the coplanar equilibrium condition; the symbols $\bar{P}_A$ and $\bar{P}_B$ have been introduced to identify the angles $\bar{P}_2 - \bar{P}_{1(2)} - \bar{P}_A$ and $\bar{P}_3 - \bar{P}_{1(3)} - \bar{P}_B$.

$$\bar{u}_{1(3)} = \tfrac{1}{2}(-\hat{l}_1 + \sqrt{3}\hat{m}_1).$$

The positions of the four carbon atoms that link the three rings, i.e., $\bar{P}_{1(2)}$ and $\bar{P}_{1(3)}$ in the parent ring and $\bar{P}_2$ and $\bar{P}_3$ in the side rings, are given by, with respect to their ring centers $\bar{R}_\xi$, $\bar{P}_{1(2)} - \bar{R}_1 = L_a \bar{u}_{1(2)}$, $\bar{P}_{1(3)} - \bar{R}_1 = L_a \bar{u}_{1(3)}$, $\bar{P}_2 - \bar{R}_2 = L_a \bar{u}_2$, and $\bar{P}_3 - \bar{R}_3 = L_a u_3$.

Finally, it is useful to define four further interaction sites, two pertaining to the parent ring, $\bar{S}_{1(2)} = \bar{R}_1 + L_c \bar{u}_{1(2)}$ and $\bar{S}_{1(3)} = \bar{R}_1 + L_c \bar{u}_{1(3)}$ and two pertaining to the side rings (2 and 3, respectively), $\bar{S}_2 = \bar{R}_2 - L_c \bar{u}_2$ and $\bar{S}_3 = \bar{R}_3 - L_c \bar{u}_3$. Here $L_c = L_a + L_b/2$, so that at the equilibrium position $\bar{S}_{1(2)} \equiv \bar{S}_2$ and $\bar{S}_{1(3)} \equiv \bar{S}_3$. The variable we have introduced will be used to simply express the different contributions to the intramolecular potential in Secs. II A–II C.

A. Stretching along the ring-ring bonds and between the side rings

The fluctuations of the distances among the centers of mass of the three rings are accounted for by introducing three ''springs.'' The parent-side ring stretching implies the elongation of a C-C bond, which is expected to have a high stiffness. The corresponding potential in harmonic approximation is written as

$$V_S = c_1[|\bar{P}_{1(2)} - \bar{P}_2| - L_b]^2 + c_1[|\bar{P}_{1(3)} - \bar{P}_3| - L_b]^2. \quad (4)$$

On the other hand, no direct chemical bond is present between the two side rings, and we expect a less stiff spring for the fluctuation of the distance between the side ring centers. We model this interaction by

$$V_B = c_2[|\bar{R}_2 - \bar{R}_3| - (2L_c)]^2. \quad (5)$$

The determination of the force constants c_1 and c_2, as well as the others we are going to introduce, will be discussed later.

B. Tilt of the ring-ring bond

In the OTP crystal structure [15], the bond angles $\bar{P}_2 - \bar{P}_{1(2)} - \bar{P}_{1(3)}$ and $\bar{P}_3 - \bar{P}_{1(3)} - \bar{P}_{1(2)}$ are 123.6° and 123.0°, respectively, while the angles $\bar{P}_2 - \bar{P}_{1(2)} - \bar{P}_A$ and $\bar{P}_3 - \bar{P}_{1(3)} - \bar{P}_B$ are 118.4° and 117.4° (see Fig. 2) Further, in the isolated molecule, the ring-ring bonds are forced out of the plane of the parent ring so that the dihedral angle $\Phi = \bar{P}_2 - \bar{P}_{1(2)} - \bar{P}_{1(3)} - \bar{P}_3$ is 5.2°. This lack of planarity is due to the little asymmetry introduced by the difference between a carbon bonded to a hydrogen and a carbon bonded to a carbon of another ring. In our model, all these angles at the equilibrium are set equal to 120° and Φ equal to 0.

We model the restoring forces for these angles by using the scalar product of the unit vectors $\bar{u}_2$ and $\bar{u}_{1(2)}$ (as well as that of $\bar{u}_3$ and $\bar{u}_{1(3)}$). Since $\bar{u}_2 \cdot \bar{u}_{1(2)} = \bar{u}_3 \cdot \bar{u}_{1(3)} = 1$ at equilibrium, the quadratic term in the small oscillation approximation is given by

$$V_{T_1} = c_3(1 - \bar{u}_2 \cdot \bar{u}_{1(2)}) + c_3(1 - \bar{u}_3 \cdot \bar{u}_{1(3)}). \quad (6)$$

However, this term is not enough to ensure the coplanarity of the vectors $\bar{u}_2$ and $\bar{u}_3$ with the parent ring; to force the rings towards the coplanar equilibrium condition we make use of the ''sites'' $\bar{S}_2$ and $\bar{S}_{1(2)}$ (as well as $\bar{S}_3$ and $\bar{S}_{13}$) introducing between them a spring of vanishing equilibrium length:

$$V_{T_2} = c_4|\bar{S}_{1(2)} - \bar{S}_2|^2 + c_4|\bar{S}_{1(3)} - \bar{S}_3|^2. \quad (7)$$

C. Rotation of the side rings along the ring-ring bond

Inside the intramolecular dynamics we expect that a crucial role is played by the rotation of the side rings planes around the ring-ring bonds [15,16] in interfering or modifying the intermolecular relaxation processes. The relevant variables describing this motion are the two angles $\{\phi_2, \phi_3\}$ between the normals to the side ring and parent ring planes. In the crystalline structure, the two side rings have slightly different angles, 42.4° and 62.0° [15]. However, we model the disordered condensed phases (liquid and glass) by using as equilibrium angle values those of the isolated molecule, i.e., 54.0°, as discussed below. We have to remark that the isolated molecule symmetry implies two isoenergetic configurations separated by a finite barrier as is qualitatively illustrated in Fig. 3. We performed an *ab initio* calculation of the single molecule potential energy surface as a function of ϕ_2 and ϕ_3 with all the other internal degrees of freedom fixed to their equilibrium values. Such calculation consists in the minimization of the Hartree-Fock energy over the Gauss-

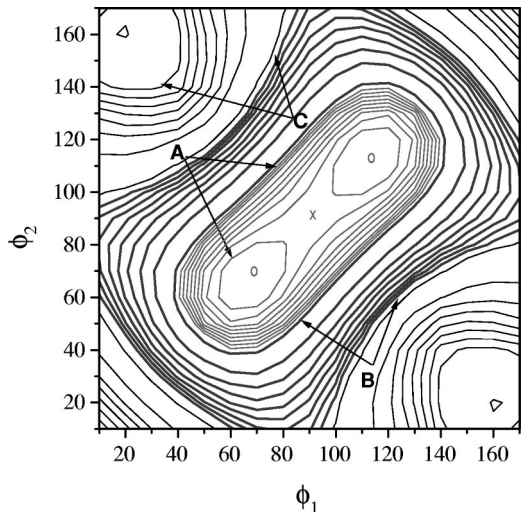

FIG. 3. Rotational energy: each point has been determined by an *ab initio* Hartree-Fock calculation of the potential energy surface as a function of the rotational angles ϕ_1 and ϕ_2 (expressed in degrees) with all the other degrees of freedom fixed to their equilibrium values; the energy is expressed in Hartree units (1 Hartree = 27.2 eV). We indicate by *A* the isolines ranging from 0.0505 to 0.0545 mHartree with an increment $\Delta_1 = 0.005$ mHartree, by *B* the ones from 0.055 to 0.095 mHartree, with $\Delta_2 = 0.05$ mHartree, and by C those from 0.5 to 1 mHartree with $\Delta_3 = 0.5$ mHartree. This figure has to be considered only from a semiquantitative point of view as explained in the text.

ian basis set 3-21G. For each atomic species the inner shell is made up of three Gaussians while the valence shell is a linear combination of two Gaussian orbitals plus one Gaussian orbital; the minimization was carried out by the standard package Gaussian 94. In Fig. 3 a contour plot of the Hartree-Fock potential energy is shown as a function of the rotation angles. It is important to quote that this map has only a semiquantitative meaning; the structure of the whole molecule is not reoptimized during the scan of ϕ_2 and ϕ_3 angles. However, a careful study, performed reoptimizing the whole molecular structure, has been done around the saddle point $\phi_2 = \phi_3 = 90°$ and around the two equivalent minima that turn out to be at $\phi_2 = \phi_3 = 54°$ and $\phi_2 = \phi_3 = 126°$. From this calculation the barrier height has been estimated to be $V_s/k_B = 580$ K and, from this value, it is possible to envisage the nature of the rotational motion at the temperatures of interest: the two side rings can pivot in phase around the bonds crossing from one minimum to the other degenerate one. Moreover, they can perform librational out-of-phase motions of (approximatively) harmonic type.

In order to represent this potential surface we express the in-phase rotation of the two side rings with a high-order (6th) polynomium and the out-of-phase rotation in the harmonic approximation. For this purpose we use as primary variables the scalar products $\overline{n_1}\cdot\overline{n_2}$ and $\overline{n_1}\cdot\overline{n_3}$ [their equilibrium value being $(\overline{n_1}\cdot\overline{n_2})_{eq} = (\overline{n_1}\cdot\overline{n_2})_{eq} = \alpha_0 = 0.59$] and to disentangle the in-phase from the out-of-phase motion, we introduce the two variables

$$\alpha = \frac{\overline{n_1}\cdot\overline{n_2} + \overline{n_1}\cdot\overline{n_3}}{2}, \tag{8}$$

$$\beta = \frac{\overline{n_1}\cdot\overline{n_2} - \overline{n_1}\cdot\overline{n_3}}{2}.$$

The final form of the ''internal rotation'' potential will be

$$V_R = V_{R_1}(\alpha) + V_{R_2}(\beta), \tag{9}$$

with

$$V_{R_1}(\alpha) = b_1\alpha^2 + b_2\alpha^4 + b_3\alpha^6, \tag{10}$$

$$V_{R_2}(\beta) = c_6\beta^2. \tag{11}$$

The parameters b_1, b_2, and b_3 describing the in-phase rotation potential are derived according to the following procedure. In the harmonic approximation, in proximity of the equilibrium position α_o for the scalar products, it must hold

$$V_{R_1}(\alpha) \approx c_5(\alpha - \alpha_o)^2, \tag{12}$$

and taking into account that the barrier height must be equal to V_s, we have the following conditions:

$$V_{R_1}(\alpha_o) = -V_s,$$

$$V'_{R_1}(\alpha_o) = 0,$$

$$V''_{R_1}(\alpha_o) = 2c_5,$$

implying

$$b_1 = -\frac{V_s}{{\alpha_o}^2} + \frac{c_5}{4} + 2b_3{\alpha_o}^4,$$

$$b_2 = \frac{c_5}{4{\alpha_o}^2} - 3b_3{\alpha_o}^2,$$

$$b_3 = \frac{1}{{\alpha_o}^4}\left(-\frac{V_s}{{\alpha_o}^2} + \frac{c_5}{4}\right). \tag{13}$$

III. FORCE CONSTANTS

We can finally write our internal model potential like

$$V_{intra} = V_S + V_B + V_{T_1} + V_{T_2} + V_{R_1} + V_{R_2}, \tag{14}$$

this potential is parametrized by the set of six free coefficients $\{c_k\}$ whose actual value can be tuned in order to obtain a *realistic free molecule vibrational spectrum*. Indeed, in the small oscillations approximation, we can determine the values of the coefficients $\{c_k\}$ by diagonalizing the dynamical matrix and fitting the resulting eigenfrequencies ω^{λ}_{DIAG} to the *lowest* frequencies ω^{λ}_{HF} obtained by a Hartree-Fock calculation of the vibrational frequencies in the electronic ground state of the isolated molecule.

We have 18 eigenvalues for the dynamics of three rings ($\lambda = 1, \ldots, 18$) but actually only $N_e = 12$ eigenvalues ω^{λ}_{DIAG} are nonvanishing, the other being associated with the translations and rotations of the molecule as a whole.

TABLE I. Values of the internal potential coefficients determined by a least square minimization of the error function, Eq. (15). The coefficients c_k are the force constants associated with the different intramolecular potential terms; the b_k, derived from the $\{c_k\}$ via the Eq. (13), describe the form of the in-phase rotational potential according to Eq. (10).

c_1	1.36×10^{-16}	J / nm^2
c_2	6.06×10^{-17}	J / nm^2
c_3	2.44×10^{-19}	J
c_4	2.65×10^{-17}	J / nm^2
c_5	4.23×10^{-19}	J
c_6	7.01×10^{-19}	J
b_1	3.62×10^{-20}	J
b_2	-4.11×10^{-19}	J
b_3	6.92×10^{-19}	J

More explicitly, the set $\{c_k\}$ is obtained by minimizing, by the standard Levenberg-Marquardt algorithm [17], the error function

$$\sum_{\lambda=1}^{N_e} (\omega_{DIAG}^{\lambda}-\omega_{HF}^{\lambda})^2 \tag{15}$$

where, for a given set of $\{c_k\}$, the quantities ω_{DIAG}^{λ} are the solution of the eigenvalues problem [18]

$$|\hat{V}-\omega^2\hat{T}|=0. \tag{16}$$

Here $\hat{V}$ and $\hat{T}$ are the Hessian matrixes of the second partial derivatives of the potential and kinetic energy, respectively, with respect to the translational and rotational degrees of freedom of the three rings.

In Table I are reported the values of the coefficients $\{c_k\}$ determined by the minimization together with the values for $\{b_k\}$ derived from Eqs. (13). The corresponding set of frequencies is shown in Table II where ω_{MD} are the frequencies derived from a computer simulation on a system of isolated molecules at low temperature. These frequencies have been identified via the peaks of the spectrum of the velocity autocorrelation function. Other model details are reported in Ref. [19].

TABLE II. Free molecule vibrational frequencies: in the second column are reported the values ω_{HF} determined by a Hartree-Fock calculation of the ground state of the isolated molecule (we consider only the 12 lowest eigenvalues); in the third column are shown the frequencies ω_{MD} corresponding to the different peaks of the spectrum determined from the atomic velocity autocorrelation function calculated by means of a preliminary molecular dynamics simulation of the isolated molecule ($\epsilon=0$) at $T=1$ K.

	ω_{HF} (cm^{-1})	ω_{MD} (cm^{-1})
1	49	55
2	54	85
3	63	99
4	97	148
5	114	165
6	140	172
7	256	273
8	271	302
9	291	306
10	358	376
11	386	409
12	428	436

IV. COMPUTATIONAL DETAILS

We have studied a system composed of 108 molecules (324 rings, 1944 interaction centers); the sample is large enough to neglect finite size effects on the investigated properties with reasonable computation times. The values of the parameters entering the site-site Lennard-Jones interactions were determined by preliminary simulations: the value of ϵ were firstly determined by comparing the computed and the experimental self-diffusion coefficients versus temperature [34] in the range $380\ \mathrm{K}\leqslant T\leqslant 440$ K; the value of σ was estimated by tuning the static structure factor so to place the first maximum in the right position [32]. Successive iterations led to $\epsilon/k_B=14$ K and $\sigma=0.4$ nm. To speed up the calculation of the intermolecular potential and to assure all the torques to be estimated in a consistent way, the cutoff for LJ interactions is applied between rings centers, i.e., the sites are considered not interacting when they pertain to rings whose center distance is larger than $r_c\simeq 3(\sigma+L_a)=1.6$ nm.

At this stage a remark about the rotational potential expressed in Eq. (9) is needed: such potential presents a serious drawback since the intrinsic ambiguity due to the parity of the scalar products involved can force the side rings in the wrong positions. This problem can be bypassed introducing a new term in the intramolecular potential that gives zero contribution to the energy when the molecule is close to the equilibrium position. If we define the product $w=(\hat{l}_1\cdot\hat{n}_2)(\hat{l}_1\cdot\hat{n}_3)$, and we set $c_7=10c_6$ (the actual value of c_7 is irrelevant, it must only be able to force the rings in the right way), we can write

$$V_A=\begin{cases} c_7 w^2 & \text{if } w>0 \\ 0 & \text{otherwise.} \end{cases} \tag{17}$$

This term has been activated only during the preparation of the initial configuration (i.e., at high temperature); during the thermalized evolution of the system we expect molecules do not drive too much away from their equilibrium configuration and then this term to be always equal to zero.

To integrate the equations of motion we have treated each ring as a separate rigid body, identified by the position of its center of mass $\overline{R_{i\xi}}$ and by its orientation expressed in terms of quaternions $\overline{q_{i\xi}}$ [20]. The standard Verlet leap-frog algorithm [20] has been used to integrate the translational motion while, for the most difficult orientational part, the refined algorithm due to Ruocco and Sampoli [21] has been employed; such choices allow a very stable integration with a relatively long time step.

The rotational dynamical problem can be written as

$$\frac{d\overline{J}_{i\xi}}{dt}=\overline{\tau}_{i\xi}(\{\overline{R}_{j\xi'}\},\{\overline{q}_{j\xi'}\}),$$
$$\frac{d\overline{q}_{i\xi}}{dt}=\hat{\mathcal{M}}(\{\overline{q}_{i\xi}\})\cdot\overline{J}_{i\xi} \tag{18}$$

where $\overline{J}_{i\xi}$ is the angular momentum of ring ξ in the molecule i, $\overline{\tau}_{i\xi}$ is the torque acting on it, and $\hat{\mathcal{M}}_{i\xi}$ is the inverse of the inertia tensor in quaternion coordinates.

The expression of the torques is simplified as the rotational part V_{rot} of the intramolecular potential energy has been expressed in terms of suitable scalar products written in the general form $s=\overline{v}_1/|\overline{v}_1|\cdot\overline{v}_2/|\overline{v}_2|$. Therefore the value of the torques τ_{v_1} and τ_{v_2} associated with the degree of freedom corresponding to the angle $\arccos(s)$ can then be evaluated by [18]

$$\tau_{v_1}=-\tau_{v_2}=-\frac{\partial V_{rot}}{\partial s}(\overline{v}_1\times\overline{v}_2). \tag{19}$$

The leap-frog algorithm for the rotational motion reported can be written in the form [21]

$$\overline{J}_{i\xi}(t+t')=\overline{J}_{i\xi}\left(t-\frac{\Delta t}{2}\right)+\overline{\tau}_{i\xi}(t)\left(\frac{\Delta t}{2}+t'\right) \tag{20}$$

with $0\leqslant t'\leqslant\Delta t$,

$$\overline{q}_{i\xi}(t+\tau)=\overline{q}_{i\xi}(t)+\int_0^\tau dt'\,\hat{\mathcal{M}}[\overline{q}_{i\xi}(t+t')]\overline{J}_{i\xi}(t+t') \tag{21}$$

with $0\leqslant\tau\leqslant\Delta t$,

$$\overline{J}_{i\xi}\left(t+\frac{\Delta t}{2}\right)=\overline{J}_{i\xi}\left(t-\frac{\Delta t}{2}\right)+\overline{\tau}_{i\xi}(t)\Delta t. \tag{22}$$

The crucial point is that the dependence of the matrix $\hat{\mathcal{M}}_{i\xi}$ on the angular variables implies the need of using a time step $\Delta t'$ to perform the numerical integration appearing in Eq. (21), smaller then Δt used for the center of mass (cm) integration. In turn, the value of Δt is limited by the highest vibrational frequency of about 450 cm^{-1}. In our case, the chosen values of $\Delta t=2$ fs and $\Delta t'=\Delta t/5$ are found to be sufficiently small to reduce the fluctuations of the total energy to a negligible fraction of the kinetic energy. It is important to note that the use of the smaller $\Delta t'$ does not increase significantly the CPU computational time since the time-consuming part in each MD step is the calculation of the forces and torques which are kept fixed during the integration of Eq. (20).

We considered a wide temperature range spanning the liquid phase and reaching the region close to T_c as shown in Table III in which the whole set of simulation times is reported. During the different temperature runs, the size of the cubic box has been rescaled in order to keep the system at the experimental density which, for $T\geqslant T_g$, can be fitted by the polynomium [22]

$$\rho(T)=1.2983-7.00\times10^{-4}T-1.23\times10^{-7}T^2, \tag{23}$$

TABLE III. Simulation runs details: at each temperature T, the system is coupled for a time t_{resc} to a stochastic heat bath, then it evolves freely, at constant energy, for a time t_{term}. At the end of this process, we consider the final configuration to be in a good equilibrium state and we start a trajectory t_{prod} ps long, saving a system configuration every t_{save} ps.

T (K)	t_{resc} (ps)	t_{term} (ps)	t_{prod} (ps)	t_{save} (ps)
443	100	1000	1000	0.1
433	100	1000	1000	0.1
420	100	1000	1000	0.1
410	100	1000	1000	0.1
389	200	1400	2000	0.1
372	200	1400	2000	0.1
351	200	1400	2000	0.1
331	500	2000	4000	0.2
321	500	3000	6000	0.3
313	500	3000	6000	0.3
300	500	3000	10 000	0.5
294	500	5000	10 000	0.5
283	500	5000	10 000	0.5

where ρ is in g/cm^3 and T in K. At each temperature T we have organized the simulations following this scheme:

The system was coupled for a time t_{resc}, chosen in a somehow arbitrary way, to a stochastic heat bath, i.e., the velocities of the rings were replaced following a logarithmic pattern with the velocities drawn from a Boltzmann distribution corresponding to such temperature.

At this point the system was at the desired temperature and we let it perform a *microcanonical* time evolution (constant energy) for a period t_{term} comparable with the experimental structural relaxation time τ_α at the same temperature; in such a way we expect every slow degree of freedom of the system to be correctly thermalized and we control that there was no drift in temperature and the degree of energy conservation (fluctuations are always less than 1% of the kinetic energy).

We considered the final system configuration obtained in this way as a good equilibrium starting state for a molecular dynamics trajectory. At each temperature we perform three different runs: the first one 20 ps long with a 4×10^{-3} ps configuration saving time has been used to compute the small-time dynamical behavior of the system; a second one 640 ps long with a 4×10^{-2} ps saving time has been used for some intermediate frequency analysis. The last one, with length t_{prod} and saving time t_{save} dependent on temperature, has been used to calculate static quantities and the long-time behavior of the system.

All the calculations have been performed on a cluster of four α-CPU with a frequency of 500 MHz; every nanosecond of simulated dynamics needed approximately 24 h of CPU time.

V. RECALL OF MAIN RESULTS FROM THE MODE-COUPLING THEORY

A great improvement to our understanding of the glassy state of matter has come from the extension of the theoretical

building of the mode-coupling theory (MCT) [2,3] developed for the *equilibrium* description of the dynamics of simple, i.e., monatomic, liquid to the study of the glassy state. Although such theory is the only microscopic approach to the glass transition leading to many predictions on the experimental data, it is still at the center of a strong debate and some questions stay open. In fact, even if the real range of validity of MCT for the study of molecular liquids has been cleared in recent years (see, among others, Refs. [23–25,44]], some experimental results seem to contradict fundamental predictions of the idealized version of MCT, such as the presence of the so-called knee characterizing the low-frequency behavior of the light scattering susceptibility [26,27] or the presence of a cusp in the nonergodicity parameter [28].

In this section we sum up the main predictions of the so-called *ideal* MCT where it is hypothesized a complete dynamical freezing and the so-called ''thermally activated hopping'' processes are neglected; such predictions will be compared with our simulation data. In the ideal MCT the glass formation is interpreted as a *dynamical transition* from an ergodic to a nonergodic behavior at a crossover temperature T_c. MCT provides a self-consistent dynamical treatment [2] for the density correlation function of an isotropic system

$$F(q,t)=\frac{1}{N}\langle \delta\rho_q^*(t)\,\delta\rho_q^*(0)\rangle, \tag{24}$$

where N is the number of the particles, $\delta\rho=\rho-\langle\rho\rangle$, $\delta\rho_q(t)=\Sigma_{i=1}^{N}\exp[i\vec{q}\cdot\vec{r}_i(t)]$, and $\vec{r}_i(t)$ is the position of particle i at time t. MCT proposes a particular *ansatz* for the memory kernel in the related integrodifferential generalized Langevin equation, such kernel is coupling nonlinearly the density fluctuations with one another. If the coupling increases upon lowering the temperature, the resulting dynamical feedback leads to a progressive slowing down of the density fluctuations until they become completely frozen at the critical temperature T_c. The ideal MCT describes the behavior as much as the temperature approaches T_c, i.e., the parameter $\sigma=(T_c-T)/T_c$ is small (however, real comparisons have to be made for σ not too small, in contrast to the case of scaling laws in phase transitions). For temperature $T\geqslant T_c$, $F(q,t)$ is characterized by two step decays taking place at different time scales and the theory gives specific predictions for such different time regions.

The first one, the *β-process* region, is centered around a time τ_σ which is predicted to scale like $\tau_\sigma\propto|T-T_c|^{1/2a}$ with $0<a<0.5$ and to be bounded in the interval $\tau_0\ll\tau_\sigma\ll\tau_\alpha$, where τ_0 is the time scale of the microscopic dynamics and τ_α is the structural rearrangement time scale. In this region the *factorization property* holds, in the sense that the density correlation function can be written as

$$F(q,t)=f(q)+h(q)\sqrt{|\sigma|}G_{\pm}(t/\tau_\sigma), \tag{25}$$

where $f(q)$ is the *nonergodicity parameter* (i.e., *Debye-Waller factor* for collective correlators or *Mössbauer-Lamb factor* for single-particle correlators), $h(q)$ is an amplitude independent of temperature and time, and the $\pm$ in $G_\pm$ corresponds to time larger or smaller with respect to τ_σ. So, the time dependence of the correlation functions is all embedded in the *q-independent* function $G_\pm$, namely spatial and temporal correlations result to be completely independent. $G_\pm(t)$ is asymptotically expressed by two power laws, respectively the *critical decay* and the *von Schweidler law* [2], characterized by the *temperature and momentum independent* exponents a and b,

$$G_\pm\left(\frac{t}{\tau_\sigma}\right)=\begin{cases}(t/\tau_\sigma)^{-a}, & \tau_0\ll t\ll\tau_\sigma\\ -(t/\tau_\sigma)^{b}, & \tau_\sigma\ll t\ll\tau_\alpha.\end{cases} \tag{26}$$

Here a is the same exponent of the power divergence of τ_σ at T_c and it is related to the exponent b $(0<b\leqslant 1)$ via the equation

$$\frac{\Gamma^2(1-a)}{\Gamma(1-2a)}=\frac{\Gamma^2(1+b)}{\Gamma(1+2b)}, \tag{27}$$

where Γ is the gamma function.

The second time region is the so-called α region where the second decaying step takes place. This region is connected to the collective structural relaxations and asymptotically the theory predicts the validity of the well-known *time-temperature superposition principle*; it states that, on time scales of the same order of magnitude as τ_α, the following scaling law holds at every temperature T:

$$F(q,t)=\mathcal{F}\left(\frac{t}{\tau_\alpha(T)}\right). \tag{28}$$

In other words, the correlation functions of any observables at different temperatures can be collapsed into a master curve when the time is scaled with t/τ_α. Moreover, MCT predicts that this master curve can be fitted by a Kolrausch-William-Watts function (*stretched exponential*)

$$F(q,t)\simeq f(q)\exp\left\{-\left(\frac{t}{\tau_\alpha}\right)^{\beta_\alpha}\right\}. \tag{29}$$

The α time scale τ_α depends on temperature through a power law of the form

$$\tau_\alpha\propto(T-T_c)^{-\gamma}, \tag{30}$$

where the *q-independent* exponent γ is related to the power exponents a and b of the β region by the relation

$$\gamma=\frac{1}{2a}+\frac{1}{2b}. \tag{31}$$

The inverse of the diffusion constant $D^{-1}(T)$ is predicted to scale like τ_α [2] and consequently it follows Eq. [30].

Up to now, all dynamical results reviewed are universal in the sense that they are predicted to hold for the correlators of every observable with nonzero overlap with density; in particular this is true for both the one-particle and the collective density correlation functions. Nevertheless important differences are predicted to hold for the q dependence in these two cases: in the former case $f(q)$ and $h(q)$ depend smoothly on q, in the latter one they oscillate, respectively, in phase and out of phase with the static structure factor $S(q)$. Moreover, β_α is predicted to be a smooth function of q in the one-

TABLE IV. Some thermodynamical results: temperatures T effectively measured, total energy E_{tot}, total potential energy V_{tot}, and kinetic energy T.

T (K)	E_{tot} (kJ/mol)	V_{tot} (kJ/mol)	T (kJ/mol)
443	30.00	-3.15 ± 0.72	33.12 ± 1.29
433	28.59	-3.78 ± 0.69	32.37 ± 1.26
420	26.88	-4.59 ± 0.69	31.47 ± 1.26
410	25.47	-5.25 ± 0.69	30.72 ± 1.20
389	22.44	-6.69 ± 0.63	29.13 ± 1.14
372	19.98	-7.83 ± 0.60	27.81 ± 1.08
351	17.10	-9.15 ± 0.57	26.28 ± 1.02
331	14.34	-10.47 ± 0.54	24.81 ± 0.96
321	12.75	-11.22 ± 0.54	24.00 ± 0.96
313	11.73	-11.67 ± 0.51	23.43 ± 0.93
300	9.96	-12.51 ± 0.51	22.47 ± 0.90
294	9.15	-12.90 ± 0.48	21.99 ± 0.90
283	7.59	-13.59 ± 0.48	21.18 ± 0.84

particle case; at variance, it shows pronounced oscillations in phase with $S(q)$ in the collective case.

VI. RESULTS

A. Thermodynamics

In this section some thermodynamical time-independent results are shown such as potential, kinetic, and total energy (see Table IV and Fig. 4). The interest in these results is clarified by the following argument: in computer simulations dealing with the glass transition it is possible to define a temperature often named T_{g-sim} [29] at which one-time quantities show some sort of discontinuity. Such discontinuity, whose position depends on the thermal history of the system, represents the thermodynamical point at which the system undergoes a glass transition on the time scale of the computer simulation, falling out of equilibrium. It is clear from Fig. 4 that no discontinuity is present, i.e., T_{g-sim} of our simulations is less than the lowest temperature studied and then we have a good chance to have well-thermalized results. Nevertheless, whether or not the system is in equilibrium can be checked only *a posteriori* by comparing the total simulation time with the measured relaxation time.

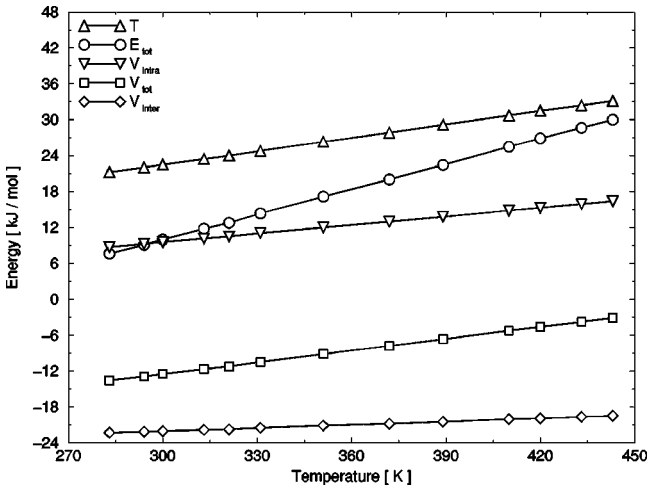

FIG. 4. Temperature dependence of the energies tabulated in Table IV, E_{tot} (circles), V_{tot} (squares), and T (triangles up) together with the internal V_{intra} (triangles down) and the intermolecular Lennard-Jones V_{inter} (diamonds) contributions to V_{tot}.

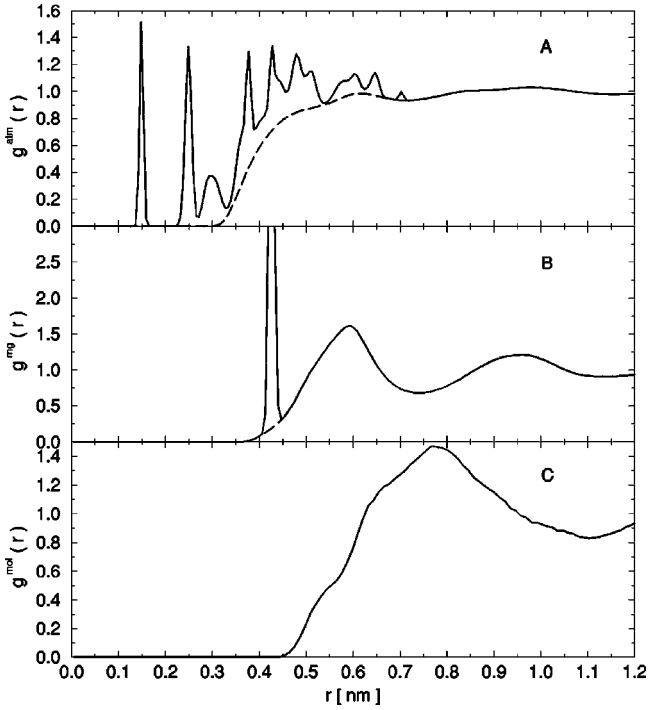

FIG. 5. Pair static distribution functions at $T=300$ K calculated on atoms (A), ring centers of mass (B), and molecular centers of mass (C); full lines represent the total contribution of both intramolecular and intermolecular distances, dashed lines only the intermolecular contribution.

From the linearity of $E(T)$ we deduce a specific heat $c(T)$ constant in the temperature range investigated and equal to $140\ \mathrm{J\,K^{-1}\,mol^{-1}}$; such value must be compared with the experimental value of $341.7\ \mathrm{J\,K^{-1}\,mol^{-1}}$ [30]. It is possible to explain the inconsistency between the two values keeping in mind that our MD value is a classical (nonquantic) result and, more important, we are neglecting many (~ 78) degrees of freedom concerning the deformations of the phenyl rings.

B. Structure

In general the static structure of a fluid is well described by the *pair distribution function* [31],

$$g(r)=\frac{V}{N^2}\left\langle \sum_i \sum_{j\neq i} \delta(r-|\overline{r_{ij}}|)\right\rangle . \tag{32}$$

In computer simulations [20], we can identify the distances $|\overline{r_{ij}}|$ with different quantities. In Fig. 5 we report some $g(r)$'s at $T=300$ K where we have considered as $|\overline{r_{ij}}|$ the distances between the carbon atoms belonging to different rings (A) and between the center of masses of rings (B) and molecules (C); both total (solid line) and intermolecular (dashed line) contributions are shown in order to separate the internal molecular structure and the mean structural organization of the whole bulk sample. In Fig. 5(B) a two peak

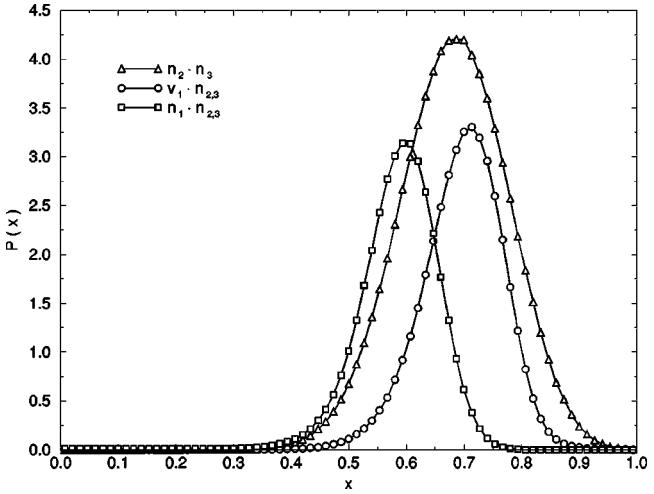

FIG. 6. Static distribution functions of the scalar products $\hat{n}_2 \cdot \hat{n}_3$ (triangles), $\hat{l}_1 \cdot \hat{n}_{2,3}$ (circles), and $\hat{n}_1 \cdot \hat{n}_{2,3}$ (squares) evaluated at $T = 280$ K.

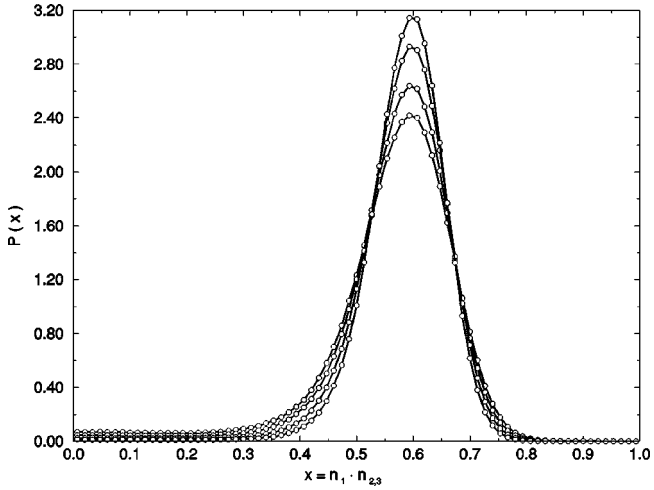

FIG. 7. Intensity of the peaks of the static distribution function of $\hat{n}_1 \cdot \hat{n}_{2,3}$ at $T = 440,390,330,280$ K (from bottom to top). An enlargement of this figure around $x = 0$ is shown in Fig. 8.

structure is present: the first sharp peak is placed at $r \simeq 0.42$ nm corresponding to the mean distance between rings belonging to the same molecule; the second one, of intermolecular origin, is placed at $r \simeq 0.6$ nm. It is worth noting that such distance is less than the greatest intramolecular C-C distance ($\simeq 0.7$ nm). Moreover, the molecular centers of mass $g(r)$ also show a large value on distances less than 0.7 nm, giving the evidence of a strong packing of the molecules. All these features appear to be approximately temperature independent. Such packing depends strongly on the orientational internal configuration of the molecules, namely on the positions of the two side rings with respect to the parent one; the computation of the probability distribution of the scalar products among the versors $\hat{l}_\xi$, $\hat{m}_\xi$, and $\hat{n}_\xi$, introduced in Sec. II, is somehow instructive in this sense.

In Fig. 6 the distribution functions for the quantities $\hat{l}_1 \cdot \hat{n}_{2,3}$, $\hat{n}_2 \cdot \hat{n}_3$, $\hat{n}_1 \cdot \hat{n}_{2,3}$ are shown. The first two distributions are practically temperature independent and give us only informations on the correctness of the simulated geometry: they are sharply peaked on the the correct equilibrium positions of about 0.71 and 0.69, respectively. At variance with the distribution of $x = \hat{n}_2 \cdot \hat{n}_3$ and of $\hat{n}_1 \cdot \hat{n}_{2,3}$ that are symmetric around $x = 0$, the distribution of $\hat{l}_1 \cdot \hat{n}_{2,3}$ does not present the symmetric peak on negative values so that we can argue that the auxiliary term V_A worked correctly. The most interesting distribution is the third one in which the peak intensity (the peak is correctly placed at $\alpha_0 = 0.59$) is higher the lower the temperature, as shown in Fig. 7, indicating therefore that the correspondent degree of freedom (the in-phase motion of $\hat{n}_1 \cdot \hat{n}_{2,3}$) is more and more frozen on its equilibrium value with decreasing the temperature.

We have seen that in the isolated molecule the rotational motion of the two side rings can be separated in two contributions: an out-of-phase harmonic libration and an in-phase pivoting around the bonds which permits rings to cross from one equilibrium position to the other degenerate one. It is clear from the structure of the distribution function in proximity of $\hat{n}_1 \cdot \hat{n}_{2,3} = 0$ shown in Fig. 8 that the time needed for the transition from a minimum to the other one will be longer lowering the temperature; moreover, Fig. 8 can be considered as a restatement of the energy map shown in Fig. 3, since the intensity of the maximum in zero is a measure of the transition probability between the two minima. Such fenomenology will be clarified in future communications where we will study the relaxation processes associated with the angular degrees of freedom.

The space Fourier transform of $g(r)$ is the *static structure factor*. In a poliatomic system this quantity is defined as

$$S(q) \propto \frac{1}{N} \sum_{i,j} b_i b_j \langle e^{i\bar{q} \cdot (\bar{r}_i - \bar{r}_j)} \rangle, \tag{33}$$

where the coefficients b_i are the *scattering lengths* in principle different for each species involved.

The $S(q)$ has been determined experimentally for OTP by neutron scattering [32,33], and the following main features have been observed.

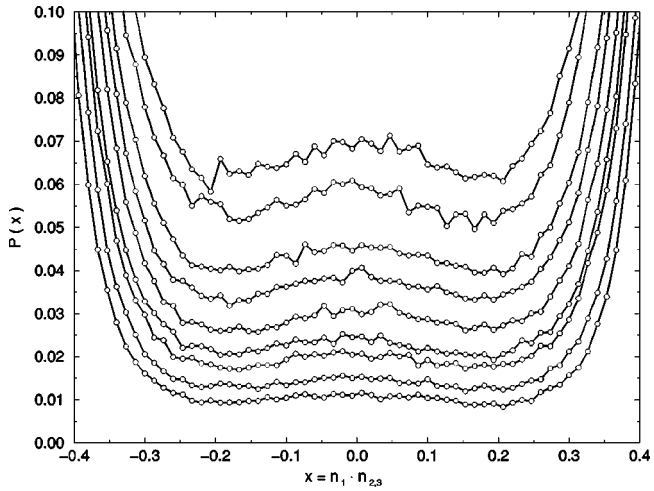

FIG. 8. Temperature dependence of the static distribution function of $\hat{n}_1 \cdot \hat{n}_{2,3}$ near the saddle point position $\hat{n}_1 \cdot \hat{n}_{2,3} = 0$ at $T = 440,420,390,370,350,330,320,300,280$ K (from top to bottom).

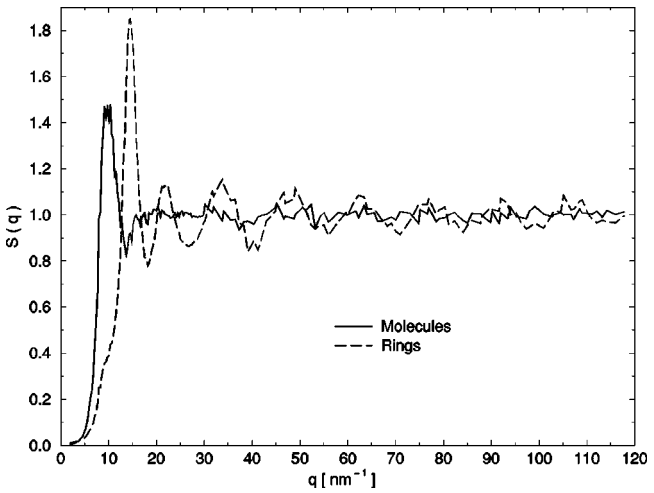

FIG. 9. Static structure factors at $T=300$ K calculated on the molecular (solid line) and ring centers of mass (dashed line); each q point is the average over all the independent Miller indices corresponding to it.

(i) In contrast to atomic systems its main peak is split in two subpeaks placed around 14 and 19 nm^{-1}.

(ii) In the $q\rightarrow 0$ region, by lowering the temperature a reduction of scattering intensity is observed due to the decrease of the isothermal compressibility χ_T [$\chi_T \propto S(q=0)$].

(iii) By increasing the density, a slight shift of the peak position to higher q values is observed.

(iv) By decreasing temperature, the height of the peak around 19 nm^{-1} increases while the intensity of the peak at 14 nm^{-1} remains nearly unaffected, except for a slight reduction mostly connected to the decrease in χ_T.

In Fig. 9 we show our results for the structure factors calculated assuming as scattering centers the molecules and the rings centers of mass with $b_i=1$; every point is an average on all the independent Miller indices corresponding to the given q.

It is much more interesting to make a comparison among the MD results and the experimental data obtained by neutron [Fig. 10(A)] and to test what is expected for x-ray scattering [Fig. 10(B)].

In evaluating $S(q)$ by computer simulation for a comparison with neutron data, we have to take into account the contribution due to both carbon and hydrogen atoms; H atoms are not considered in our dynamics; nevertheless, it is possible to place them in fixed positions on the line extending from the center of the ring through a carbon atom at a fixed C-H distance computed to be $d_{\text{C-H}}=0.107$ nm. In this case we would have to consider different scattering lengths for the two species, b_{H} and b_{C}; nevertheless, they are both positive and about the same magnitude so that the product $b_i b_j$ in Eq. (33) is an ineffective constant.

In Fig. 10(A) the calculated $S(q)$ at $T=300$ K is shown and compared with the data of Ref. [32] at $T=324$ K; in this paper the authors show their results in terms of the *coherent scattering cross section* $(d\sigma/d\Omega)$ measured in m^2 which is proportional to our $S(q)$. In order to compare the two results we renormalized the experimental data in such a way the values of the two curves coincide at large q. The high-q region of the calculated $S(q)$ appears to be in excellent agreement with the experiment but no double peak structure

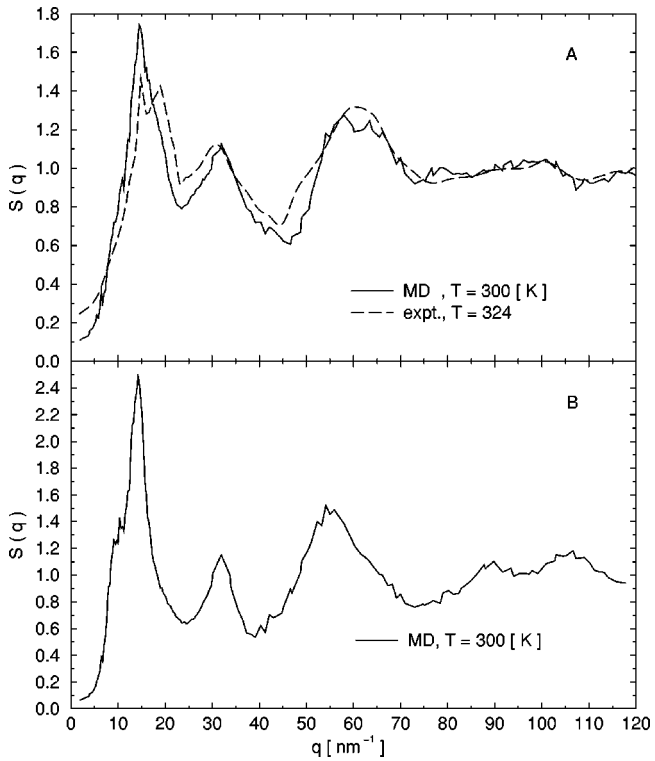

FIG. 10. Top: Comparison among molecular dynamics structure factor (solid line) calculated taking into account both carbon and hydrogen atoms as scattering centers and experimental structure factor (dashed line) measured by neutron scattering (from [32]). Bottom: Molecular dynamics structure factor (solid line) calculated taking into account only carbon atoms; this should be the correct result to be compared with the experimental structure factor measured by x-ray scattering.

is present at low momenta. In particular the MD calculated first peak presents a small bump at about 18 nm^{-1}; this is better seen in Fig. 11 where we show the small-q part of $S(q)$ calculated at $T=280$ K together with the error bars estimated by means of the statistical fluctuation of the data. The noise cannot allow us to determine the correct structure

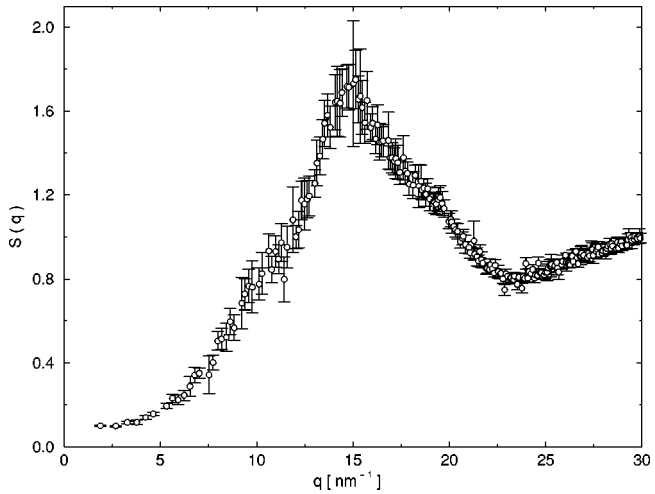

FIG. 11. Enlargement of the low-momenta region of $S(q)$ calculated at $T=280$ K: the error bars are estimated from the fluctuation of the single configuration $S(q)$'s.

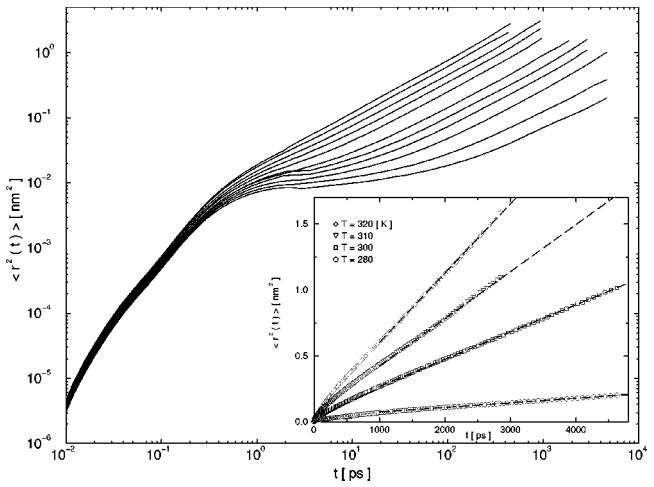

FIG. 12. Temperature dependence of the mean-square displacement $\langle r^2(t)\rangle$ calculated on ring centers of mass at all temperature investigated except $T=440,420$ K (higher temperature on top). Inset: linear scale plot of the mean-square displacement at some selected temperatures (open symbols) together with the long-time linear behavior (dashed lines).

of the main peak. It is worth noting, moreover, that at this low temperature the characteristic relaxation time is of order 1 ns, so that, considering a simulation run 10 ns long, we have only about ten really independent system configurations.

In order to calculate the simulated $S(q)$ as is expected by x-ray scattering, we consider only the carbon atoms; also in this case no double-peak structure is observed in the data but a clear prepeak appears at a q value less than the q of the first maximum, since the high-q behavior is similar to the neutron case, as shown in Fig. 10(B).

C. Self-diffusion coefficient

An important quantity to consider in the study of the dynamics of our system at a microscopic level is the *mean-squared displacement* (MSD) defined as

$$\langle r^2(t)\rangle = \frac{1}{N}\sum_{i\xi}\langle|\overline{R}_{i\xi}(t)-\overline{R}_{i\xi}(0)|^2\rangle, \tag{34}$$

where $\overline{R}_{i\xi}(t)$ is the position of the center of mass of the ring ξ in the molecule i at time t; from the MSD is possible to determine the *self-diffusion coefficient* $D(T)$ via the Einstein relation

$$D=\lim_{t\to\infty}\frac{1}{6t}\langle r^2(t)\rangle. \tag{35}$$

The temperature dependence of the MSD is shown in Fig. 12; each curve follows the usual *cage-effect* scenario. At small time (less than 0.2 ps) they present the t^2 behavior corresponding to the ballistic motion; at long time the diffusive linear time dependence of Eq. (35) is found. At intermediate times a small region is present where MSD stays almost constant and whose duration increases with decreasing temperature; on these time scales molecules are trapped in cages built up by their neighbors, and they can only vibrate in these limited regions, the length of the plateau being a measure of the mean lifetime of the cages.

TABLE V. Temperature dependence of the molecular dynamics self-diffusion coefficient D.

T (K)	$10^7\times D$ (cm^2/s)
443	106.2
433	89.3
420	81.3
410	66.6
389	49.3
372	37.3
351	27.3
331	12.5
321	9.4
313	6.3
300	3.4
294	0.8
283	0.6

The calculated values of the self-diffusion coefficient are shown in Table V and plotted in Fig. 13 (open circles) as a function of temperature, together with the power-law temperature dependence (solid line) predicted by the MCT

$$D^{-1}(T)\propto(T-T_c)^{-\gamma}. \tag{36}$$

A three parameters fit to these data has been performed obtaining the following values:

$$T_c^{(D)}=278\pm3, \tag{37}$$

$$\gamma^{(D)}=1.8\pm0.1, \tag{38}$$

In the same figure we also show the experimental data (full squares) [34,35] that are well represented by Eq. (36) (dashed line) with the values $\gamma=2.3\pm0.1$ and $T_c=292\pm2$ K.

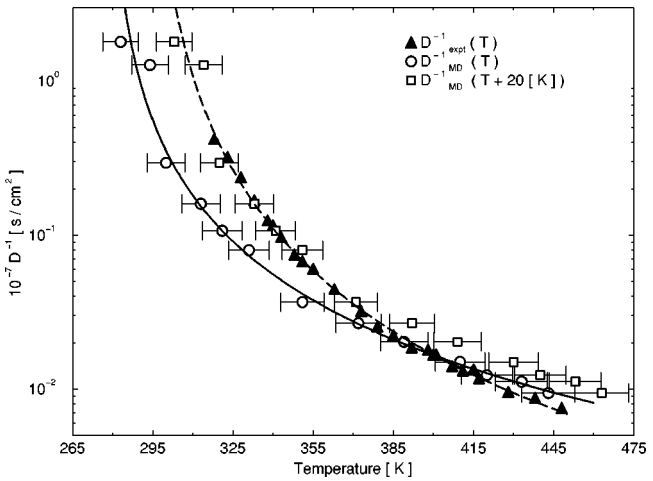

FIG. 13. Temperature dependence of molecular dynamics (open circles) and experimental (full triangles) diffusion coefficients together with the power-law fits in the form of Eq. (36) (solid and dashed lines, respectively); we show also the MD data shifted of 20 K (open squares) as explained in the text.

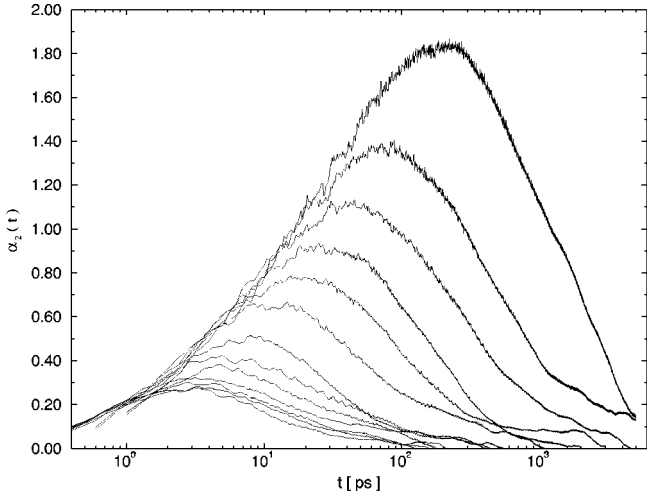

FIG. 14. Time dependence of the non-Gaussian parameter $\alpha_2(t)$ for all temperature investigated (lower temperatures on top).

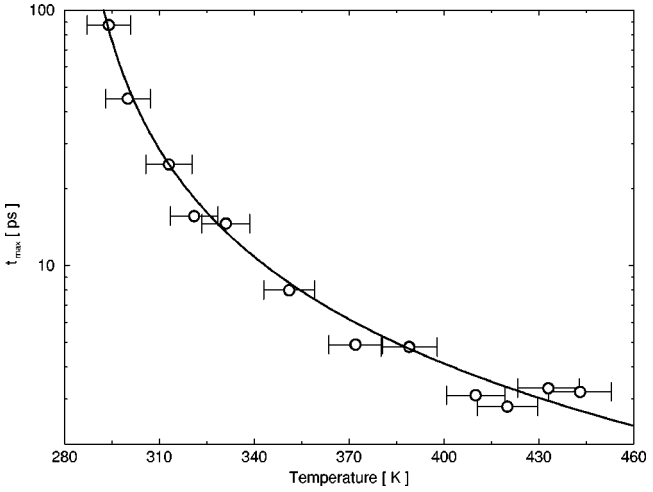

FIG. 15. Power-law fit of the temperature dependence of the position t_{max} of the maximum of the non-Gaussian parameter.

It is clear from these values and from Fig. 13 that a discrepancy is present among the lower temperatures diffusive behavior of the simulated and real system, respectively; this is most likely due to the fact that we have tuned the value of the LJ potential parameters ϵ and σ in order to reproduce the high-T diffusion properties of the real system. However, it is worth noting that it is possible to reproduce quite well the experimental results on the whole investigated temperature range shifting the molecular dynamics points at temperatures ~ 20 K above their true values. In other words, we have to assume that our actual thermodynamic point is shifted with respect to the real one; from now on, whenever we will compare our molecular dynamics results with the experimental ones, our calculated points will be shifted 20 K above the measured temperature and the competing temperatures will be indicated as $\overline{T}_c$. On these grounds from the previous study of the self-diffusion properties of our model we obtain $\overline{T}_c^{(D)}=298\pm 3$ to be compared with the experimental value $T_c=290\pm 5$.

A different way to determine the parameters entering in the power law reported in Eq. (36) is possible, even if not independent from the previous one; it is based on the study of the *non-Gaussian* parameter $\alpha_2(t)$ defined as [36,37]

$$\alpha_2(t)=\frac{9}{5}\frac{\langle r^4(t)\rangle}{\langle r^2(t)\rangle^2}-1, \tag{39}$$

where the mean-square displacement $\langle r^2(t)\rangle$ and $\langle r^4(t)\rangle$ are, respectively, the second and forth momenta of the *Van Hove self-correlation function*

$$G_s(\overline{r},t)=\frac{1}{N}\sum_{i\xi}\langle \delta(\overline{r}-\overline{R}_{i\xi}(t)+\overline{R}_{i\xi}(0))\rangle. \tag{40}$$

The parameter $\alpha_2(t)$ quantifies the degree of non-Gaussianity of $G_s(\overline{r},t)$ in space as a function of time and it is normalized in such a way that, if $G_s(\overline{r},\tilde{t})$ was a Gaussian function in space at a given time $\tilde{t}$, we would have $\alpha_2(\tilde{t})=0$. The time dependence of $\alpha_2(t)$ at all temperatures investigated is shown in Fig. 14. We are not interested here in the specific time dependence of such function but only in the fact that $t_{\alpha_{max}}$, the position of the maximum of $\alpha_2(t)$, has the power dependence on T similar to that of Eq. (36) [36] (see Fig. 15). A fit to this quantity performed in the same way as before gives us the values

$$\overline{T}_c^{t_\alpha}=300\pm 14, \tag{41}$$

$$\gamma^{t_\alpha}=1.4\pm 0.3, \tag{42}$$

compatible with the values determined by the temperature dependence of D, even if the error bars are larger in this case.

D. Single particle dynamics

Comparisons of the *coherent* (collective) and *incoherent* (self-) density fluctuations dynamics data measured by different techniques (neutron time-of-flight and backscattering spectroscopy, photon correlation spectroscopy, depolarized Raman and Rayleigh-Brillouin light scattering) with the main predictions of MCT have been reported in literature with great details [38–43]. In this section we will study the single particle density fluctuation dynamics of our model and we will compare our results with the experimental results mainly contained in Refs. [38,39] and with the MCT predictions.

The single particle dynamics of the model is embedded in the *incoherent self-intermediate scattering function* defined as

$$F_s(q,t)=\frac{1}{N}\left\langle \sum_{i,\xi} e^{-i\overline{q}\cdot[\overline{R}_{i\xi}(t)-\overline{R}_{i\xi}(0)]}\right\rangle \tag{43}$$

where, again, $\overline{R}_{i\xi}(t)$ is the position of the center of mass of the ring ξ in the molecule i at time t. At every temperature considered two sets of configurations, produced with two different storing times as described in Sec. IV, have been used to reconstruct the whole curve. We considered the T dependence of $F_s(q,t)$ at the two momentum values $q=14{,}19$ nm^{-1} corresponding to the first and second peaks of the static structure factor, averaging on values of q falling in the interval $q\pm\Delta q$ with $\Delta q=0.2$ nm^{-1}. Finally, we

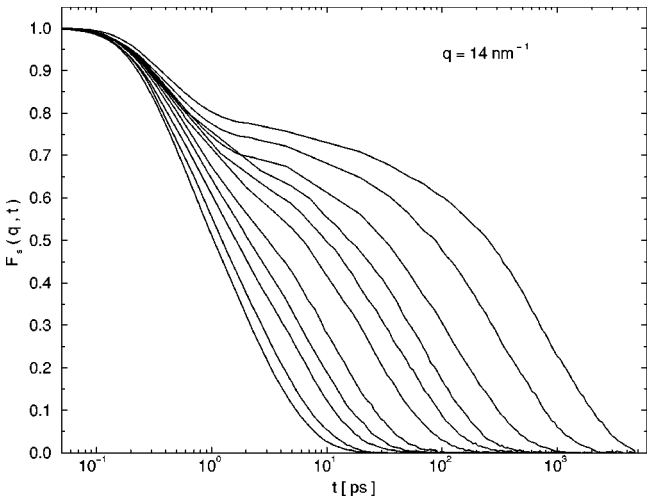

FIG. 16. Temperature dependence of $F_s(q,t)$ calculated at $q=14$ nm^{-1} for all temperatures investigated except $T=410,430$ K (lower temperatures on top).

spanned at $T=300$ K the whole interesting q space in the interval $q=2\div 30$ nm^{-1} (averaging on the values of q falling in the same interval $2\Delta q$ wide).

In Fig. 16 we show $F_s(q,t)$ for nearly all temperatures investigated at $q=q_{max}=14$ nm^{-1}; all the curves decay to zero, i.e., the length of all the simulations allows the fluctuations to become completely uncorrelated. We are in a ''good'' thermodynamical equilibrium at every temperature, at least on the space scales corresponding to the inverse of q_{max}.

At temperatures lower then $T=330$ K the relaxation follows clearly the predicted two step pattern: on microscopic time scales the correlation is quadratic in time, this timescale being the one on which the intramolecular vibrations happen; on intermediate time scales we observe the formation of a plateau, whose height is the nonergodicity parameter $f(q)$ and whose length in time is comparable to the one of the plateau in the MSD $\langle r^2(t)\rangle$. On long-time scales we observe the structural relaxation in the form of a stretched exponential. At the highest temperatures no double pattern is visible anymore and only a nearly exponential relaxation can be recognized. A stretched exponential fit [see Eq. (29)] on the structural time scale (α process) gives us the temperature dependence of the three free parameters β_α, τ_α, and $f(q)$.

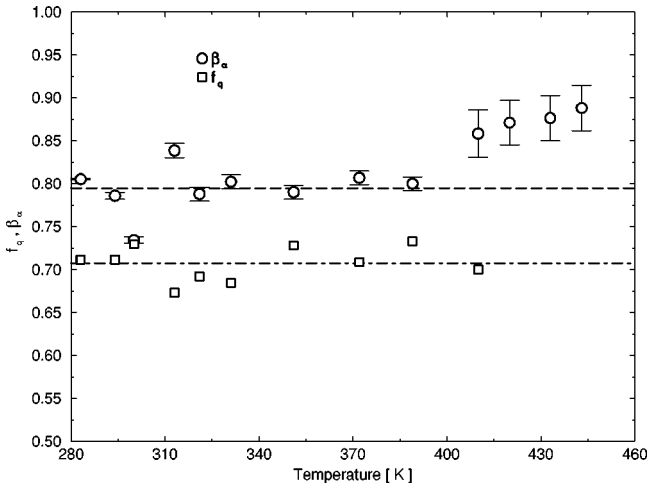

FIG. 17. Temperature dependence of the stretching parameter β_α (circles) and of the nonergodicity parameter f_q (squares); the horizontal lines indicate the mean values of β_α (dashed line) and f_q (dot-dashed line).

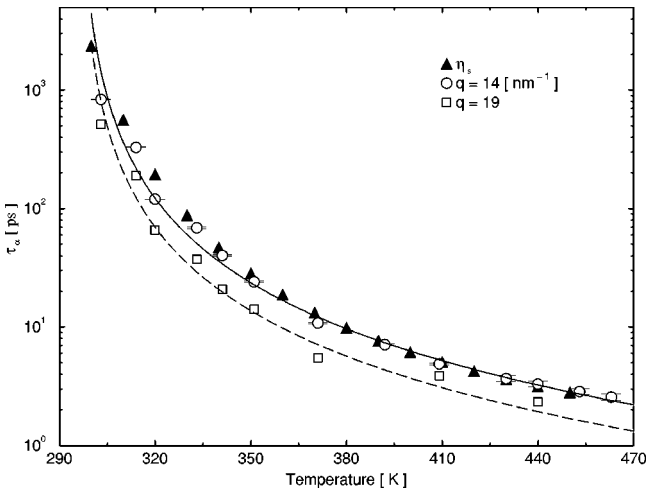

FIG. 18. Temperature dependence of τ_α at $q=14,19$ nm^{-1} (circles and squares, respectively) together with the power-law fits with $\overline{T}_c^{\tau_\alpha}=296$ K and $\gamma^{\tau_\alpha}=2.0$ (solid and dashed lines, respectively); also the experimental shear viscosity $\eta_s \propto \tau_\alpha$ data (full triangles) are reported (see [22] and reference therein) multiplied by a factor 1.5 ps/Poise. Molecular dynamics results have been shifted 20 K with respect to the measured temperatures, as explained in text.

The parameter β_α (circles) is shown in Fig. 17; it appears to be nearly T independent for temperature lower than $T=400$ K and its mean value $\beta_\alpha \simeq 0.8$ (dashed line) has to be compared with the experimental value $\beta_\alpha=0.6$. For temperature in the higher region it tends toward the value $\beta_\alpha=1$ (errors are clearly much more greater); such behavior is due to the fact that in this temperature region it is no longer possible to sharply separate the long-time relaxation region from the microscopic short-time one. The study of the temperature dependence of the nonergodicity parameter $f(q)$ in the interesting region is not possible due to our limited tem-

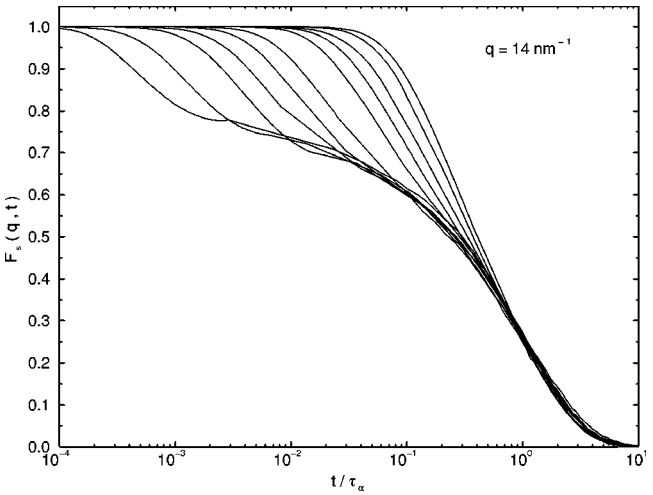

FIG. 19. $F_s(q,t)$ at $q=14$ nm^{-1} rescaled to t/τ_α; all the curves verify the time-temperature superposition principle.

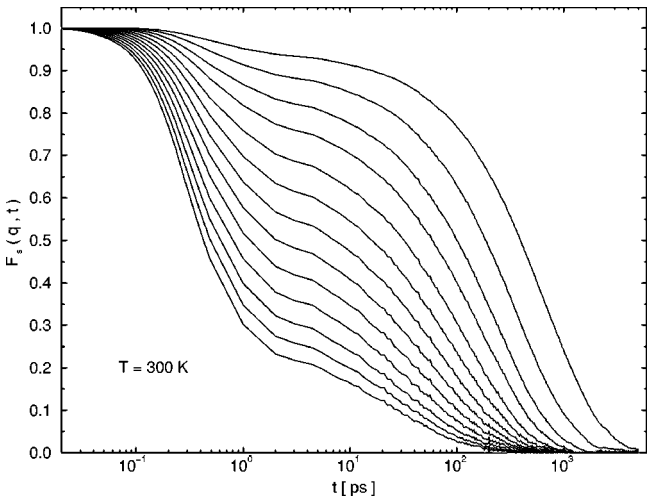

FIG. 20. Q-dependence of $F_s(q,t)$ at $T=300$ K for $q=2n$ nm^{-1} with $n=3,\ldots,15$ (from top to bottom).

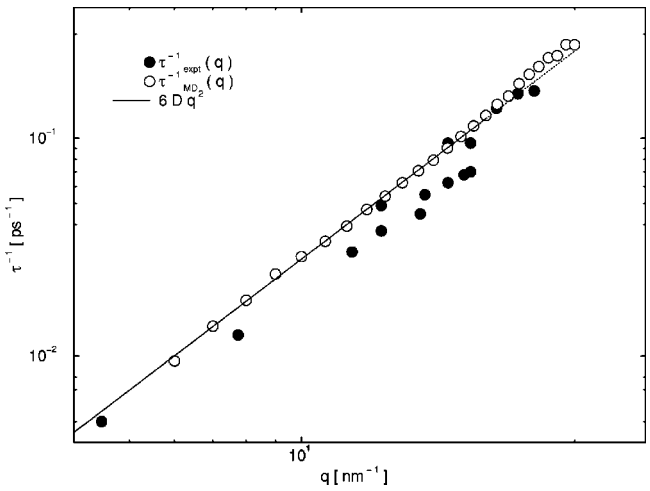

FIG. 22. Q-dependence of the inverse relaxation time τ_α^{-1}; molecular dynamics data (open circles) have been multiplied by a factor 6.5 in order to overlap the experimental [38] data (full circles), as explained in the text. The solid line is the correct small-q behavior $\tau_\alpha^{-1}(q)\simeq 6Dq^2$, where $6D=20.4\times10^{-5}$ nm^2/ps.

perature range which do not permit to observe the expected low-temperature ($T<T_g$) harmonic Debye-like behavior, and the onset of the anomalous decrease of $f(q)$ with increasing T for $T_g<T\leqslant T_c$. Our data suggest us $T_c<283$ K and the mean value $f(q)\simeq0.7$ (dot-dashed line) agrees with the experimental value determined at $T=290$ K shown later in Fig. 21.

It is worth testing the power-law temperature dependence Eq. (30) for the relaxation time τ_α; the calculated relaxation times (circles) shifted 20 K with respect to the measured temperatures, as explained above, are plotted in Fig. 18 together with the experimental (full triangles) *shear viscosity* η_s data (η_s is expected to be proportional to τ_α) of Ref. [22] and the theoretical fitted curve (solid line) of parameters

$$\overline{T}_c^{\tau_\alpha}=296\pm7, \tag{44}$$

$$\gamma^S=2.0\pm0.4 \tag{45}$$

to be compared with the experimental results of Ref. [38], $T_c=290\pm5$ K and $\gamma=2.55$. These values are compatible, within the statistical error, with the values calculated from the diffusion data, so we can conclude that the diffusive behavior and the self-dynamics of our model follow the same *critical* power law with $\overline{T}_c\simeq297$ K and $\gamma\simeq1.8$.

Also the values of τ_α for $q=19$ nm^{-1} (squares) corresponding to the second peak of the static structure function are reported with the theoretical curve. A fit has been performed (dashed line) only on the prefactor keeping fixed the values of the other two parameters in order to show that these data also are compatible with the same power law. The crucial observation here is that the values of the two parameters T_c and γ are effectively q independent and they can be considered universal for our model, as predicted by the MCT.

The relaxation time τ_α can be also used to test the time-temperature superposition principle Eq. (28). In Fig. 19 the curves are shown in function of the rescaled time t/τ_α and it is clearly seen that all the curves tend to collapse on the same master curve as predicted by the theory.

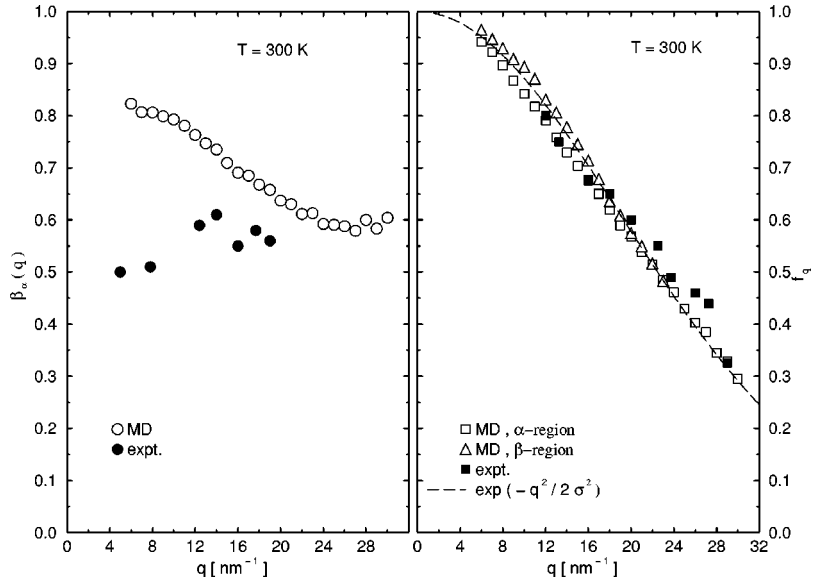

FIG. 21. Q dependence of the stretching and non-ergodicity parameters: Left: molecular dynamics (circles) and experimental (filled circles, from [38]) values of the coefficient β_α as determined by the stretched exponential fits. Right: experimental values (filled squares) of the nonergodicity parameter [38] together with the molecular dynamics results as determined by a MCT analysis of both α (squares) and β (triangles) regions and the Gaussian fit (solid line) to α-region results with $\sigma^2=365$ nm^{-2}.

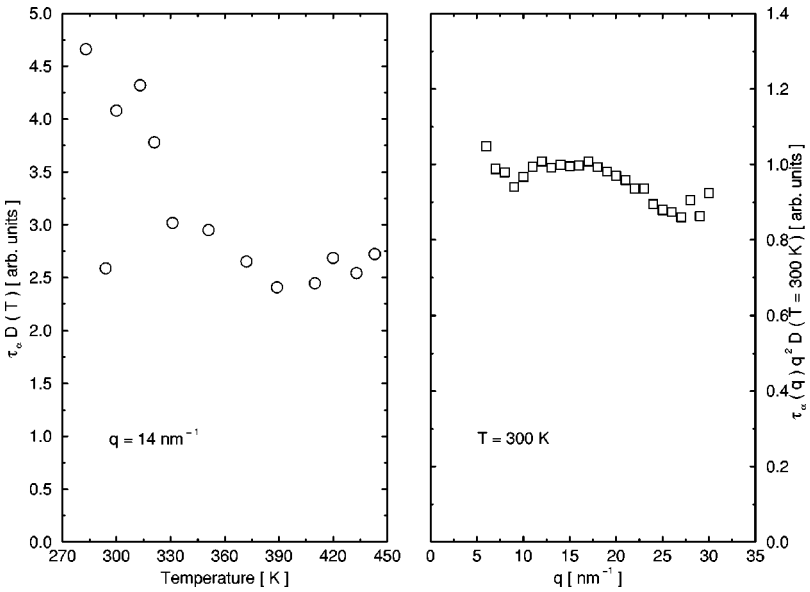

FIG. 23. Left: Temperature dependence of the product $\tau_\alpha D$ at $q=1.4$ nm^{-1}. Right: q dependence at $T=300$ K of $\tau_\alpha D q^2$. These quantity are expected to be constant.

We now quantify the q dependence of the self-dynamics long-time behavior of the system at $T=300$ K. In Fig. 20 are reported the curves $F_s(q,t)$ for values of $q=2n$ nm^{-1} with $n=3,\ldots,15$; the choice of the temperature value $T=300$ K has been due to the need of ''well-thermalized'' results in a large range of q. Also in these data are the well-defined two-step behavior and we can calculate the long-time stretched exponential fit parameters; the resulting values are shown in Figs. 21 and 22. In Fig. 21 the values of β_α (left side) and $f(q)$ (right side) are shown.

β_α (open circles) appears to be a smooth function of q and it tends, for large values of q, to the experimental (full circles) evaluated value of 0.6. Such behavior is quite general (see, for instance, Ref. [37]) and can be easily explained by the following argument [37]: for large values of q, corresponding to length scales of the same order of magnitude of the cages dimension, the dynamics becomes slower and slower approaching the cage dynamics described through the von Schweidler exponent b. At variance, in the opposite limit of small q, we consider a diffusive dynamics on large distances; at such length scales the decay of the self-density fluctuations is of the usual purely exponential form $\exp(-Dq^2t)$ corresponding to $\beta_\alpha=1$ (see Fig. 27). At this stage, however, we have not a reasonable explanation of the disagreement with the experimental data.

In the right side of Fig. 21 the q dependence of the nonergodicity parameter $f(q)$ is also shown as calculated from the short-time limit of the α process (squares), from the long-time part (triangles) of the β region (as we will see below), and from the experimental data (full squares) [38]; it seems clear a good agreement between our values and the experimental results. The data appear to be monotonic decreasing as increasing q and this dependence is expected to be approximately Gaussian; in Fig. 21 a Gaussian fit (solid line) in the form $\exp(-q^2/2\sigma^2)$ with $\sigma\simeq 19$ nm^{-1} to the molecular dynamics α region data is also shown. It is clear that the q range considered here is too limited to really decide on the validity of this functional form (a linear approximation would work well too), a good estimate of the error bars lacking in this case.

In Fig. 22 the q dependence of τ_α^{-1} is shown (circles) together with the experimental data [38] (full circles). Molecular dynamics points have been rescaled by a factor $\tau_\alpha^{MD}(T=280\ \text{K})/\tau_\alpha^{MD}(T=300\ \text{K})\simeq 6.5$ to take into account the fact, as discussed above, that our system temperature is 20 K higher than the real one. The correct square-law behavior at low-q $\tau_\alpha^{-1}(q)\simeq 6Dq^2$ [see Eq. (47)] is also shown as a solid line; here D is the self-diffusion coefficient and $6D=20.4\times10^{-5}$ nm^2/ps.

Finally, in Fig. 23, two products of some calculated quantity, expected to be constant, are shown; on the left-hand side the statement $D^{-1}(T)\propto\tau_\alpha(T)$ is proven for $q=q_{max}$ (good at highest temperature). On the right-hand side we show the product $\tau_\alpha q^2 D$ evaluated at $T=300$ K, which is nearly constant up to $q\simeq 18$ as expected, this value being approximately the crossover point among the correct quadratic behavior and the asymptotically linear regime as we found above.

Let us now probe the MCT conclusions about the *β region* which is predicted to follow the power laws of Eq. (26):

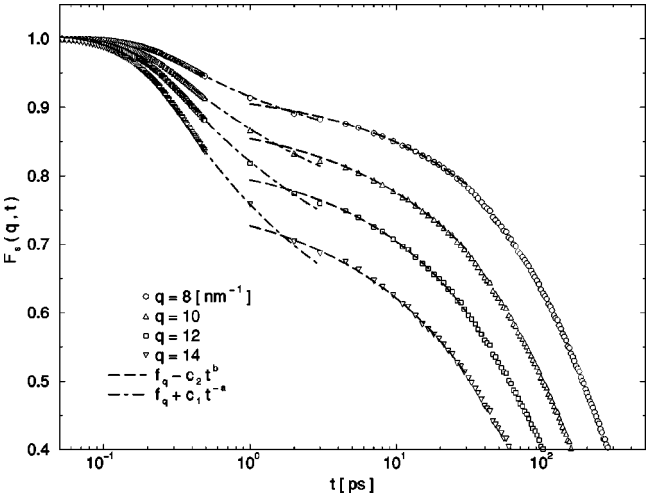

FIG. 24. Power laws in the β region for $q=8,10,12,14$ nm^{-1}; critical decay of exponent a (dot-dashed lines) and the von Scweidler law of exponent b (dashed lines) have been reported with simulation points.

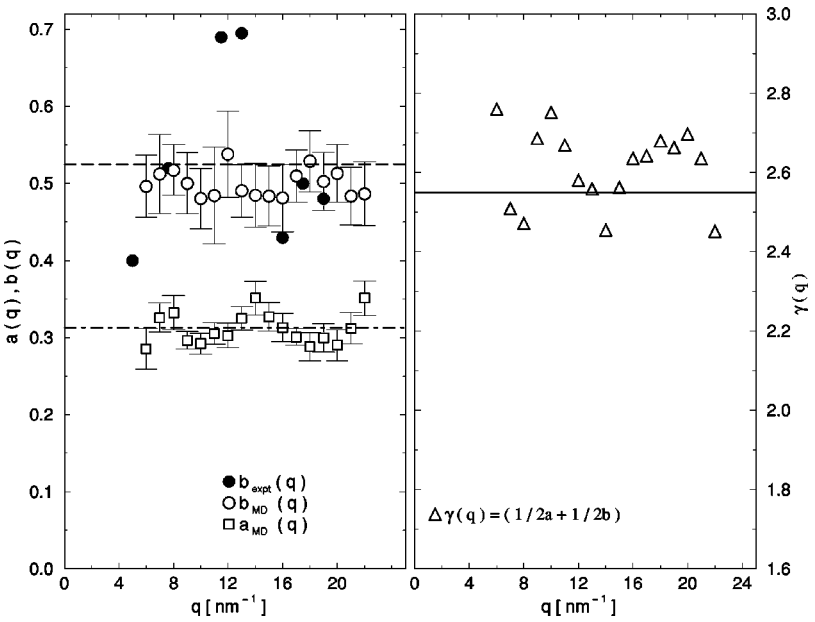

FIG. 25. Q dependence of the power-laws exponents. Left: the experimental values (filled circles) for $b(q)$ are plotted together with the molecular dynamics values for $b(q)$ (open circles) and $a(q)$ (open squares); the mean values for our results are shown by the dashed and dot-dashed lines, respectively. Right: our values for the q dependence of the exponent γ determined by the relation $\gamma = 1/2a + 1/2b$.

we show here the results at fixed temperature $T=300$ K for values of $q=6+n$ nm^{-1} with $n=0,\ldots,17$.

We fit all the curves by two power functions on the time ranges θ_1 and θ_2,

$$F_s(q,t)=\begin{cases} f_q+c_1 t^{-a}, & t\in\theta_1 \\ f_q-c_2 t^{b}, & t\in\theta_2 \end{cases} \tag{46}$$

where $\theta_1=[0.15:2]$ (ps) and $\theta_2=[3:20]$ (ps); some selected fits are shown in Fig. 24 and they seem to work quite well.

Some observations are needed on the following analysis: a great uncertainty stems from the choice of the fit range (i.e., from the choice of θ_1 and θ_2) due to the consideration of a crossover region between two processes not sharply separated in time; moreover, an analogous problem cannot be excluded between the microscopic region and the critical decay region characterized by the exponent a. Such difficulty implies a great uncertainty on the determination of $f(q)$ which is supposed to be considered as the long-time limit of the β process and the short-time behavior of the α relaxation. At this point it is clear that, lacking a careful error analysis on the data points, such fits can only state that a parametrization of the data in the form of Eq. (46) is possible which is consistent with the theory predictions [39], the current values of the determined parameters being considered only from a qualitative point of view.

Nevertheless the values of such fitting parameters, shown in Figs. 25 and 26, appear to be in good agreement with the values obtained from the experimental data. In Fig. 25 are shown (left) the values of the power exponents a (squares) and b (circles) and of the exponent γ (triangles) calculated by means of Eq. (31) (right side); the mean values are 0.3, 0.5, 2.6, respectively, to be compared with the experimental determined values $a\simeq 0.31$ (dot-dashed line), $b\simeq 0.52$ (dashed line), $\gamma\simeq 2.55$ (solid line) [38].

It is clear from these results that one of the main predictions of MCT, namely the q independence of a and b is verified in the limit of the error fluctuations. Moreover, it is important to note that the parameter γ, given by Eq. (31), remains constant, as expected, being its mean value 2.6 is clearly compatible with the value 2.55 determined from experimental data [38]; nevertheless, this value overestimates the value $\gamma=2.0\pm 0.4$ at $q=14$ nm^{-1} previously determined by the fit to the α region. Furthermore, $b(q)$ is always less than the determined value of the large-q value of the stretching parameter $\beta_\alpha=0.6$ (see Fig. 21) verifying another MCT prediction, namely $0<b<\beta_\alpha$.

From Eqs. (25), (26), and (46) the two parameters $c_1(q)$ and $c_2(q)$ result to be proportional to $h(q)$, the proportionality constants being dependent on σ, τ_σ, a, and b. From $T_c\simeq 280$ K we have $\sqrt{\sigma}\simeq 0.3$ while we choose as a good estimate of τ_σ the intersection point of the two power laws of Fig. 24, obtaining $\tau_\sigma\simeq 2$ ps; if we put $a=0.31$ and $b=0.52$ we finally obtain the factors 2.7 and 2.3 for c_1 and c_2, respectively.

Unfortunately these value are not able to correctly rescale our data on the experimental results, the correct values being 0.7 and 4 as shown in Fig. 26; this result could be expected considering the great uncertainties on the parameter values used for the estimate. Nevertheless, simulated data agree quite well with the experimental points at low-q presenting a strong bending toward a constant value in the region $q>16$ nm^{-1}.

To complete the picture of the self-motion in our model, we test the validity of the *Gaussian approximation* to $F_s(q,t)$ in the limit of small momentum q. The first-order term of the expansion of $F_s(q,t)$ in powers of q^2 gives [31]

$$F_s(q,t)\simeq\exp\left\{-\frac{q^2}{6}\langle r^2(t)\rangle\right\}. \tag{47}$$

In Fig. 27 some curves at $T=330$ K and different values of q are shown together with the corresponding approximations; such approximation seems to work quite good and it becomes worse on increasing q as expected.

At the end, we show in Fig. 28 all the time scales related to centers of mass motion investigated up to now as a function of temperature. Full circles and squares indicate, respectively, the experimental structural relaxation time $\tau_{expt}^{V-F}(T)$,

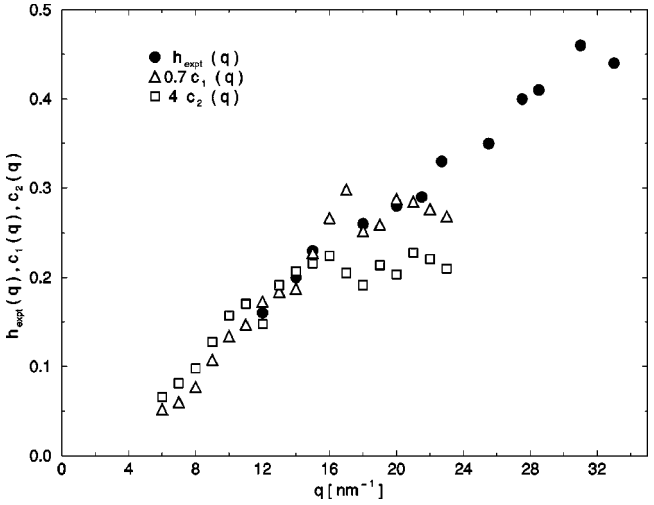

FIG. 26. Q dependence of the experimental (full circles) coefficient h of Eq. (25) and of our fitting parameters c_1 (triangles), c_2 (squares); note that our results have been rescaled by a factor 0.7 and 5, respectively in order to superimpose to experimental data.

following the Vogel-Fulcher law, and the experimental inverse self-diffusion coefficient $D_{expt}^{-1}(T)$ multiplied by a factor 5×10^{-5} cm^2 in order to superimpose to $\tau_{expt}^{V-F}(T)$. The open symbols are used to represent the molecular dynamics results: τ_{MD}^{s} (diamonds) is the relaxation time of the one-particle dynamics at $q=14$ nm^{-1} multiplied by a scale factor 1.5 and $D_{MD}^{-1}(T)$ (triangles up) is the inverse of the diffusion coefficient rescaled by the same factor 5×10^{-5} cm^2 we used for the experimental points. All the molecular dynamics points have been shifted of 20 K with respect to the measured temperatures; it is quite clear that both experimental and molecular dynamics data points collapse on a well-defined master curve. Our model is, at least, a good model for centers of mass dynamics of OTP.

VII. CONCLUSIONS

In this paper we have introduced an interaction potential model capable of describing the intramolecular dynamics of

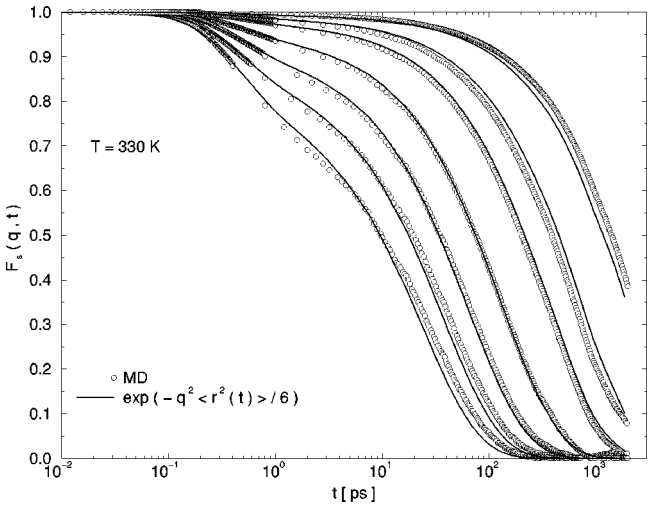

FIG. 27. Gaussian approximation to $F_s(q,t)$ at $T=330$ K for $q=2,3,4,6,8,1,1.2$ nm^{-1} (from top to bottom).

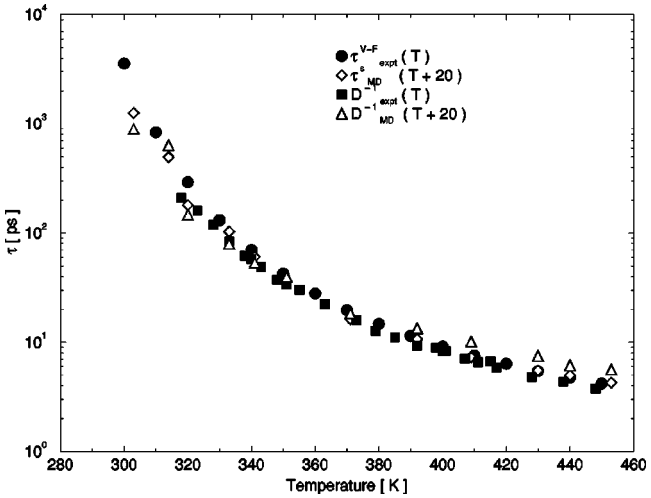

FIG. 28. Master plot of the temperature dependence of all the centers of mass time scales discussed: we have used full symbols for experimental results and open symbols for molecular dynamics data. Molecular dynamics points collapse exactly on the master curve identified by the experimental data if they are multiplied by a scale factor (taking into account the momentum dependencies of the relaxation time τ_{MD}^{s} and the correct dimensionality of the diffusion coefficients) and the corresponding temperatures are shifted 20 K above the measured ones, as discussed in the text. In particular, τ_{MD}^{s} (open diamonds) is multiplied by a factor 1.5, and the self-diffusion coefficients D_{expt}^{-1} (full squares) and D_{MD}^{-1} (open triangles) are rescaled by a factor 5×10^{-5} cm^2.

the fragile glass-former OTP; such a model appears to be much more efficient with respect to the ones introduced so far in the sense that it represents a much better compromise between the resulting computing needs and its capability to mimic all the complexities of the dynamical behavior of the real system.

It takes into account not only the translational and rotational dynamics of the molecules as a whole but also the stretching along the molecular bonds, and the tilt of the bonds, the rotations of the side rings with respect to the parent ring. It is tuned in such a way to reproduce the isolated molecule vibrational spectrum. In this way, most likely, we have introduced the degrees of freedom whose interplay causes the complex dynamical behavior of the real system. We have, then, presented the results of molecular dynamics computer simulations of such a model; we mainly studied the static structure of a bulk sample, the self-diffusion properties, and the self-part of the density-density correlation functions.

The static structure factor simulated in such a way is compared with the experimental measures and shows a good agreement with the neutron scattering data, except for the very low momenta behavior (due, probably, to the finite size of our system). Moreover, we have no evidence of the splitting of the main peak in two subpeaks placed at $q=14,19$ nm^{-1}, only the first one being clearly visible. This luck may be due mainly to the temperature range investigated (the intensity of the second subpeak increases with lowering temperature).

The self-diffusion properties of the system have been investigated through the mean-squared displacement and the self-diffusion coefficient temperature behavior; comparisons

with experimental self-diffusion data give a very good agreement, showing the evidence of compatible critical dynamics behavior in approaching the instability temperature T_c of MCT which is here found to be $T_c = 278 \pm 3$ to be compared with the experimental value $T_c = 290 \pm 5$ determined by a MCT analysis of the dynamics of the density fluctuations, a discrepancy which is most to likely ascribed to the intermolecular LJ potential parameters (σ, ϵ) that have been tuned in the temperature region close to $T = 300$ K. Moreover, we considered the critical temperature dependence of the so-called non-Gaussianity parameter $\alpha_2(t)$ obtaining compatible values for the power-law parameters.

The self-dynamics of the density fluctuations has been studied in great detail on the whole accessible time window, spanning the range from a time scale of the order of few femtoseconds to times of order of some nanoseconds; moreover, its dependence on temperature and momenta has been investigated. All the correlation curves calculated show the typical two step behavior predicted by MCT, the first one on short time being associated with the so-called ''microscopic'' processes, i.e., the vibrational motion of molecules in the cage built up by their neighbors; the second one being associated with the α process which controls the structural rearrangements of molecules on a long-time scale.

The critical dynamics on an α time scale approaching the correspondent T_c is in good agreement with experimental findings; indeed the estimate values for our model of the exponent $\gamma = 2.0 \pm 0.4$ must be compared with the experimental value $\gamma = 2.5$.

The q dependence at $T = 300$ K in the momentum range $q = 6 - 30$ nm^{-1} has been analyzed in terms of a stretched exponential fit; the values of the determined parameters are in good agreement with the ones calculated by fitting the experimental points and with the MCT expected behavior.

To summarize, in the present work we have shown that our model for OTP fluid is mimicking rather well the center of mass dynamical features of the real system, giving results in most cases fully compatible with the experimental findings. It is clear that its ability to help us in the understanding of the most exotic dynamic features of the real systems and, in particular, of the relevance of the internal degrees of freedom on the translational dynamics, has not been fully displayed in this paper; problems such as the collective dynamics density fluctuation behavior, the rotational dynamics, the origin of the unusual fast relaxational dynamics, and many others, will be addressed in future works [19].

ACNOWLEDGMENTS

The authors wish to thank W. Götze for a critical reading of the manuscript, L. Bernardini and G. Giuliani of the ''Parco Tecnologico d'Abruzzo'' for technical support, G. Monaco and F. Sciortino for some useful discussions.

[1] C. A. Angell, Science **267**, 1924 (1995).
[2] W. Götze, in *Liquids, Freezing and the Glass Transition*, edited by J. P. Hansen, D. Levesque, and J. Zinn-Justin (North-Holland, Amsterdam, 1991); W. Götze and L. Sjörgen, Rep. Prog. Phys. **55**, 241 (1992); W. Götze, J. Phys.: Condens. Matter **11**, A1 (1999).
[3] R. Schilling, in *Disorder Effects on Relaxational Processes*, edited by A. Richert and A. Blumen (Springer-Verlag, Berlin, 1994); W. Kob, in *Experimental and Theoretical Approaches to Supercooled Liquids: Advances and Novel Applications*, edited by J. Fourkas *et al.* (ACS Books, Washington, 1997).
[4] K. L. Ngai and K. Y. Tsang, Phys. Rev. E **60**, 4511 (1999).
[5] M. Mézard and G. Parisi, Phys. Rev. Lett. **82**, 747 (1999).
[6] F. Sciortino, W. Kob, and P. Tartaglia, J. Phys.: Condens. Matter **12**, 1 (2000).
[7] G. Monaco, D. Fioretto, C. Masciovecchio, G. Ruocco, and F. Sette, Phys. Rev. Lett. **82**, 1776 (1999).
[8] G. M. Brown and H. A. Levy, Acta Crystallogr., Sect. B: Struct. Crystallogr. Cryst. Chem. **35**, 785 (1979).
[9] S. Aikawa, Y. Maruyama, Y. Ohashi, and Y. Sasada, Acta Crystallogr., Sect. B: Struct. Crystallogr. Cryst. Chem. **34**, 2901 (1978).
[10] A. Criado, F. J. Bermejo, A. de Andres, and J. L. Martinez, Mol. Phys. **82**, 787 (1994).
[11] J. J. Ou and S. H. Chen, J. Comput. Chem. **19**, 86 (1998).
[12] G. Wahnström and L. J. Lewis, Physica A **201**, 150 (1993); L. J. Lewis and G. Wahnström, Solid State Commun. **86**, 295 (1993); J. Non-Cryst. Solids **172-174**, 69 (1994); Phys. Rev. E **50**, 3865 (1994).
[13] C. M. Roland, K. L. Ngai, and L. J. Lewis, J. Chem. Phys. **103**, 4632 (1995); C. M. Roland and K. L. Ngai, *ibid.* **106**, 1187 (1997); F. Sciortino and P. Tartaglia, J. Phys.: Condens. Matter **11**, A261 (1999).
[14] S. R. Kudchadkar and J. M. Wiest, J. Chem. Phys. **103**, 8566 (1995).
[15] W. R. Busing, J. Am. Chem. Soc. **104**, 4829 (1982).
[16] D. H. Wertz and N. L. Allinger, Tetrahedron **35**, 3 (1979).
[17] G. E. Forsythe, M. A. Malcolm, and C. B. Moler, *Computer Methods for Mathematical Computations* (Prentice-Hall, Englewood Cliffs, NJ, 1976).
[18] H. Goldstein, *Classical Mechanics* (Addison-Wesley, Reading, MA, 1965).
[19] S. Mossa, Ph.D. thesis, Università di L'Aquila, 1999.
[20] M. P. Allen and D. J. Tildesley, *Computer Simulation of Liquids* (Clarendon Press, Oxford, 1989).
[21] G. Ruocco and M. Sampoli, Mol. Phys. **82**, 875 (1994).
[22] G. Monaco, Ph.D. thesis, Università di L'Aquila, 1998.
[23] L. Fabbian, A. Latz, R. Schilling, F. Sciortino, P. Tartaglia, and C. Theis, Phys. Rev. E **60**, 5768 (1999).
[24] S. Kämmerer, W. Kob, and R. Schilling, Phys. Rev. E **56**, 5450 (1997).
[25] T. Franosch, M. Fuchs, W. Götze, M. R. Mayr, and A. P. Singh, Phys. Rev. E **56**, 5659 (1997).
[26] J. Wiedersich, T. Blochowicz, S. Benkhof, A. Kudlik, N. V. Surovtsev, C. Tschirwitz, V. N. Novikov, and E. Rössler, J. Phys.: Condens. Matter **11**, A147 (1999).
[27] J. Gapinski, W. Steffen, A. Patkowski, A. P. Sokolov, A. Kisliuk, U. Buchenau, M. Russina, F. Mezei, and H. Schober, J. Chem. Phys. **110**, 2312 (1999).
[28] F. Mezei and M. Russina, J. Phys.: Condens. Matter **11**, A341 (1999).

[29] W. Kob and H. C. Andersen, Phys. Rev. E **51**, 4626 (1995).
[30] S. S. Chang and A. B. Bestful, J. Chem. Phys. **56**, 503 (1972).
[31] J. P. Hansen and J. R. Mc Donald, *Theory of Simple Liquids* (Academic Press Limited, London, 1986).
[32] E. Bartsch, H. Bertagnolli, P. Chieux, A. David, and H. Sillescu, Chem. Phys. **169**, 373 (1993).
[33] A. Tölle, H. Schober, J. Wuttke, and F. Fujara, Phys. Rev. E **56**, 809 (1997).
[34] D. W. McCall, D. C. Douglass, and D. R. Falcone, J. Chem. Phys. **50**, 3839 (1969).
[35] F. Fujara, B. Geil, H. Sillescu, and G. Fleischer, Z. Phys. B: Condens. Matter **88**, 195 (1992).
[36] T. Odagaki and Y. Hiwatari, Phys. Rev. A **43**, 1103 (1991).
[37] F. Sciortino, P. Gallo, P. Tartaglia, and S. H. Chen, Phys. Rev. E **54**, 6331 (1996).
[38] W. Petry, E. Bartsch, F. Fujara, M. Kiebel, H. Sillescu, and B. Farago, Z. Phys. B: Condens. Matter **83**, 175 (1991).
[39] M. Kiebel, E. Bartsch, O. Debus, F. Fujara, W. Petry, and H. Sillescu, Phys. Rev. B **45**, 10 301 (1992).
[40] E. Bartsch, F. Fujara, J. F. Legrand, W. Petry, H. Sillescu, and J. Wuttke, Phys. Rev. E **52**, 738 (1995).
[41] A. Tölle, J. Wuttke, H. Schober, O. G. Randl, and F. Fujara, Eur. Phys. J. B **5**, 231 (1998).
[42] Y. Hwang and G. Q. Shen, J. Phys.: Condens. Matter **11**, 1453 (1999).
[43] W. Steffen, A. Patkowski, H. Gläser, G. Meier, and E. W. Fischer, Phys. Rev. E **49**, 2992 (1994).
[44] R. Schilling and T. Scheidsteger, Phys. Rev. E **56**, 2932 (1997).